

44 **Abstract**

45 Characterizing the physico-chemical properties of dust-emitting sediments in arid regions is
46 fundamental to understanding the effects of dust on climate and ecosystems. However, knowledge
47 regarding high-latitude dust (HLD) remains limited. This study focuses on analyzing the particle size
48 distribution (PSD), mineralogy, cohesion, iron (Fe) mode of occurrence and Visible Near Infra-Red
49 (VNIR) reflectance spectra of dust-emitting sediments from dust-hotspots in Iceland (HLD region).
50 Extensive analysis was conducted on samples of top sediments, sediments and aeolian ripples
51 collected from seven dust sources, with particular emphasis on the Jokulsá basin, encompassing the
52 desert of Dyngjunsandur. Both fully and minimally dispersed PSDs and their respective mass median
53 particle diameters revealed remarkable similarities (56±69 and 55±62 μm, respectively). Mineralogical
54 analyses indicated the prevalence of amorphous phases (68±26 %), feldspars (17±13 %), and
55 pyroxenes (9.3±7.2 %), consistent with thorough analyses of VNIR reflectance spectra. The Fe content
56 reached 9.5±0.40 wt %, predominantly within silicate structures (80±6.3 %), complemented by
57 magnetite (16±5.5 %), hematite/goethite (4.5±2.7 %), and readily exchangeable Fe-ions or Fe nano-
58 oxides (1.6±0.63 %). Icelandic top sediments exhibited coarser PSDs compared to the high dust-
59 emitting crusts from mid-latitude arid regions, distinctive mineralogy, and a threefold bulk Fe content,
60 with a significant presence of magnetite. The congruence between fully and minimally dispersed PSDs
61 underscores reduced particle aggregation and cohesion of Icelandic top sediments, suggesting that
62 aerodynamic entrainment of dust could also play a role upon emission in this region, alongside
63 saltation bombardment. The extensive analysis in Dyngjunsandur enabled the development of a
64 conceptual model to encapsulate Iceland's rapidly evolving high dust-emitting environments.

65
66
67 **Keywords:** Arid regions, Iceland dust sources, Arctic desert, High latitude dust, Sediments, Size and
68 Composition, Spectroscopy, Dust modelling

69
70
71
72
73
74
75
76
77
78
79
80
81
82
83
84
85

Eliminado: For
Eliminado: , this knowledge is scarce

Eliminado: top sediments

Eliminado: -sources

Eliminado: and an intensive

Eliminado: at

Eliminado: including top sediments, sediments and aeolian ripples...

Eliminado: F

Eliminado: evidenced

Eliminado: with an average median diameter of

Eliminado:

Eliminado: showed

Eliminado: aligned

Eliminado: the

Eliminado: mainly in

Eliminado: have

Eliminado: large

Eliminado: a

Eliminado: may

Eliminado: aside of

Eliminado: of an extensive sampling in

Eliminado: allowed

Eliminado: this study to present a conceptual model

Eliminado: -

Eliminado:

Eliminado: D

113 **1. Introduction**

114 Dust particles created by wind erosion of arid surfaces can traverse considerable distances, spanning
115 continents and oceans, and influencing the Earth's climate (Kok et al., 2023). The impact of dust on
116 climate and the environment strongly depends upon its particle size distribution (PSD), composition,
117 and shape, which to a large extent are determined by the properties of the parent source of sediments
118 (Perlwitz et al., 2015; Gonçalves et al., 2023). While most of the dust is produced in hot, arid,
119 subtropical sources like the Sahara (Kok et al., 2021), and most studies have concentrated on these
120 regions, dust produced in cold high-latitude environments, defined as dust emitted from latitudes \geq
121 50° N and $\geq 40^\circ$ S, receives increasing attention due to its regional and potentially global significance,
122 and sensitivity to global warming (Bullard et al., 2016; Meinander et al., 2022). High-latitude dust
123 (HLD) is emitted from regions such as Iceland, Greenland, Svalbard, Alaska, Canada, Antarctica, New
124 Zealand, and Patagonia. Its physical, chemical and optical properties can differ strongly from those of
125 crustal dust produced in lower latitude sources, and affect, among other, atmospheric (Johnson et al.,
126 2010), marine (Jickells et al., 2005), and cryospheric (Oerlemans et al., 2009) processes.

127 Numerous geological processes, especially glacial and periglacial ones, and volcanic activity, occurring
128 in high latitude regions promote the emission of contemporary dust (Bullard, 2013; Bullard et al.,
129 2016). Initially, large volumes of volcanic fine volcanic ash are deposited and trapped by glacier ice
130 over geological epochs, later released as sediment into glacial rivers upon glacier retreat. Moreover,
131 the physical weathering of rocks by glaciers produces a vast amount of silt and sand, transported from
132 beneath glacial margins by glacial rivers (Palacios et al., 2022). Additionally, during dust events, fine
133 dust is deposited and trapped within glacier ice, re-emerging as sediment during melting. Eventually,
134 these glacial rivers discharge from the glacier, forming floodplains where the silt and sand accumulate,
135 facilitating dust emission to the atmosphere by strong winds. Such regions are common in Iceland,
136 and include Dyngjúsandur, Skeiðarársandur, Mælifellssandur and Mýrdalssandur (Arnalds et al.,
137 2001). Glaciers like Vatnajökull, Iceland's and Europe's largest, additionally face significant ice loss due
138 to climate change. Models suggest that warming rates of $\geq 2^\circ\text{C}$ per century could result in a 50%
139 reduction in ice cap volume and area within 200 years (Flowers et al., 2005), eventually increasing the
140 amount of sediment released into glacial rivers. Besides warming, factors such as volcanic activity
141 contribute to accelerated melting and frequent sediment-laden flooding events, followed by rapid
142 drying and subsequent dust emissions.

143 As it could be expected melting is accelerated in summer and at midday (Carrivick and Tweed, 2019).
144 Thus, with insolation the melting increases, and then the glacier fluvial discharges reach a maximum
145 after midday, causing frequent flooding episodes during the afternoon. After the flooding the high
146 permeability of these sediments favors a fast infiltration of the ponded waters, followed by a fast
147 drying of the surfaces. During the next days, in the morning drying of the surfaces and convective
148 and/or synoptic winds favors the emissions of dust.

149 In Iceland, active volcanoes erupt every 3-5 years, depositing thick layers of tephra ranging from
150 millimetres to centimetres (Arnalds et al., 2016). This deposition process has the potential to lead to
151 the formation of new dust sources when new basalt fields obstruct river flows and create ephemeral
152 lakes. All these processes together make Iceland one of the most active dust hotspots in the world,
153 with $>20,000$ km² of sandy deserts ($\approx 20\%$ of Iceland) exposed to aggressive aeolian activity releasing
154 millions of tonnes of dust to the atmosphere (Arnalds et al., 2016; Baldo et al., 2020). Icelandic dust is

- Eliminado: shape,
- Eliminado: and
- Eliminado: its
- Eliminado: associated
- Eliminado: Kok et al., 2023
- Eliminado: but

- Eliminado: ,
- Eliminado: and
- Eliminado: its

- Eliminado: geophysical
- Eliminado: ,
- Eliminado: under current environmental conditions favor
- Eliminado: P
- Eliminado: that is
- Eliminado: underneath
- Eliminado: the
- Eliminado: s
- Eliminado: At a certain point
- Eliminado: flow out
- Eliminado: and
- Eliminado: are deposited
- Eliminado: enabling
- Eliminado: .

Eliminado: Additionally, in active volcanic regions, massive volumes of volcanic ash can be trapped by ice in glaciers across geological history and be supplied as sediment to the glacial rivers upon melting

182 emitted, transported and deposited over land, sea, and ice of the North Atlantic, covering areas in
183 Iceland, north-western Europe, north-eastern America and Greenland (Arnalds et al., 2014; Baldo et
184 al., 2020). Icelandic dust can reduce surface albedo and either increase or decrease melting of glaciers
185 and ice caps via deposition depending on the deposited layer thickness (Dragosics et al., 2016;
186 Wittmann et al., 2017; Möller et al., 2016, 2018). Icelandic dust is also rich in iron (Fe) (e.g. Arnalds et
187 al., 2014), which depending on its mode of occurrence can exert different climate and ecological
188 effects. Fe-oxide minerals strongly absorb solar radiation (Formenti et al., 2014; Engelbrecht et al.,
189 2016; Di Biagio et al., 2019; Zubko et al., 2019), potentially contributing to direct radiative effects in
190 the Arctic (Kylling et al., 2018). The deposition of soluble Fe from Icelandic dust to the ocean can
191 impact Fe biogeochemistry and primary productivity in the subpolar North Atlantic Ocean, which is
192 seasonally Fe limited (Arnalds et al., 2014). Icelandic dust can also be a sporadically important source
193 of ice-nucleating particles (INP) at mid to high latitudes (Sanchez-Marroquin et al., 2020; Shi et al.,
194 2022), relevant to the cloud-phase climate feedback (Murray et al., 2021).

195 Desert dust can also affect air quality, and accordingly human health (Goudie & Middleton, 2006; De
196 Longeville et al., 2010; Karanasiou et al., 2012; Pérez García-Pando et al., 2014). Thorsteinsson et al.
197 (2011) reported ambient concentrations of atmospheric particulate matter (PM) <10 µm (PM₁₀) higher
198 than 100 µg/m³, on a 30 min basis, during various dust storms in Reykjavik, with dust transport from
199 the Landeyjarsandur area (100 km ESE of the capital). Dagsson-Waldhauserova et al. (2016) reported
200 mean 5-minute average PM₁₀ and PM₁ levels of 158-583 and 97-241 µg/m³, respectively at
201 Landeyjarsandur, and 7-486 µg/m³ PM₁₀ at Hagavatn (both major dust hotspots, [Figure 1](#)). Dagsson-
202 Waldhauserova et al. (2015) reported similar PM₁₀ levels in Reykjavik, but higher in
203 Kirkjubæjarklaustur (up to 6500 µg/m³, 1 min basis).

204 Dyngjusandur, Dyngjuvatn, Hagavatn, Mælifellsandur, Mýrdalssandur, Landeyjarsandur and
205 Skaftarsandur (Figure 1) are the most active dust emission areas in Iceland (Arnalds, 2020). The
206 emission of dust from these regions depends on the season. In the long cold periods, the snow cover
207 prevents dust emissions (Arnalds, 2010). After thawing, soil moisture hinders dust emission;
208 nonetheless, during summer (mostly August) there is a higher probability for dust emission, especially
209 in inland areas, such as Dyngjusandur (Figure 1), where the periodic passage of fronts from the Arctic
210 and low pressure systems are common and are associated with high wind speed, generally between
211 5 and 15 m/s, with peaks of up to 30 to 50 m/s, 10 m height (Einarsson, 1984, Olafsson et al., 2007).

212 Glaciofluvial sediments in Iceland may exhibit distinct particle size characteristics. Samples collected
213 in Dyngjusandur, Hagavatn, Landeyjarsandur, Mælifellsandur, Myrdahlsandur, and Sandkluftavatn
214 generally display unimodal distributions with a notably diverse profile, featuring average diameters
215 ranging from 20 to 98 µm (Meinander et al., 2022). Icelandic dust is mostly made up of basaltic
216 particles (Baratoux et al., 2011; Thorpe et al., 2019). The dust-emitting sediments mainly consist of
217 volcanic glass, with minor proportions of anorthite (0-20 %), augite (0-10 %), and traces of forsterite,
218 microcline, Ti-magnetite and quartz (Baldo et al., 2020). Wada et al. (1992), reported the occurrence
219 of plagioclase, augite, halloysite, allophane and imogolite in sediment samples at Thingvallasveit,
220 Myrdalur, Biskupstungnaafrettur and Godafoss; while Thorpe et al. (2019) that of plagioclase, augite,
221 olivine, volcanic glass and secondary minerals in soil samples at Hvítá. Baratoux et al. (2011) reported
222 that dust near Dyngjusandur was made up of 80-90 % of volcanic glass, and traces of pyroxene, olivine
223 and plagioclase, and that from Lambrahaun was made up of 0-20 % of volcanic glass with very high

Eliminado:

Eliminado: s

Eliminado: s

Eliminado: in

Eliminado: the soils have too much moisture to be able to emit...

Eliminado:

231 plagioclase and olivine contents. Dagsson-Waldhauserova et al. (2015) showed that a deposited dust
232 sample from a top snow layer in Reykjavik reflected the major basaltic composition of the source
233 lands, with mean values of 40-50 % SiO₂, 14-20 % Al₂O₃, 8-16 % CaO, 2-4 % Na₂O + K₂O, 4-9 % MgO,
234 10-17 % FeO and 0.8-5 % of TiO₂, which is in concordance with that of PM₁₀ and PM₂₀ obtained by
235 resuspension of sediment samples in a chamber (Baldo et al. 2020). Dagsson-Waldhauserova et al.
236 (2015) also showed that deposited dust from Mælifellsandur and Skeidarársandur were similar in
237 composition, with 42-45 % SiO₂, 14-15 % Al₂O₃, 11-12 % CaO, 4.0-4.1 % Na₂O + K₂O, 4.9-6.2 % MgO,
238 14-17 % FeO and 3.5-5.6 % of TiO₂.

239 Several atmospheric modelling studies have already attempted at representing HLD (Thorsteinsson et
240 al., 2011; Groot Zwaafink et al., 2017; Beckett et al., 2017; Cvetkovic et al., 2022; Meinander et al.,
241 2022). However, the inclusion of HLD in Earth system models is only at its early stages (Shi et al., 2022),
242 and it is currently a challenge. While the fundamental processes governing aeolian dust emissions in
243 HLD should be broadly consistent with those in temperate regions, many HLD source regions exhibit
244 additional or amplified processes unique to their environment. These include the highly dynamic
245 nature of many of HLD sources, their potential expansion driven by glacier melting and retreat in a
246 warming climate (Meinander et al., 2022), the potentially distinct emission mechanisms, and different
247 physicochemical properties. Currently, there is a lack of information on the PSD and mineralogy of
248 dust sources to feed model simulations of emission and transport of dust for climate and
249 environmental impact assessment (Laurent et al., 2008; Perlwitz et al., 2015a and b; Kok et al., 2021).
250 This is especially evident for HLD, where dust observations are scarce (Cvetkovic et al., 2022) and
251 mineralogical maps for dust modelling are not available (Claquin et al., 1999; Journet et al., 2014;
252 Green et al., 2020). Specifically, the size and mode of occurrence of Fe require investigation
253 (Mahowald et al., 2005). It is known that hematite/goethite increases the radiative forcing of dust
254 whereas nano Fe-oxides and easily exchangeable Fe might increase the fertilising effect of dust in
255 ocean and terrestrial ecosystems (Baldo et al., 2020). However, magnetite has different wavelength-
256 dependent optical properties than hematite/goethite (Matsui et al., 2018), and for Icelandic dust it
257 might be the principal contributor to its radiative absorption effect on climate. Also, the high
258 proportions of volcanic glass can influence the radiative forcing of Icelandic dust (Baldo et al., 2023).
259 All in all, there is a pressing need for an improved understanding of the formation and distribution of
260 sediments in HLD hotspots, encompassing an in-depth examination of their compositional and
261 physical attributes. Specifically, a characterization of the PSD, mineral composition, the mode of
262 occurrence of Fe and Visible Near Infra-Red (VNIR) reflectance spectral signatures is essential for
263 accurate representation of HLD sources and the associated dust effects in forthcoming Earth System
264 models. The analysis of both minimally disturbed PSD (MDPSD) and fully disturbed PSD (FDPSD) can
265 further help in understanding the degree of particle aggregation and sediment cohesion (González-
266 Romero et al., 2023), which should contribute towards understanding and constraining dust emission
267 schemes in these regions.

268 This study aims at investigating the major patterns of sediments and processes that account for the
269 high dust emission in Dyngjusandur (Figure 1), one of the most active dust emission areas in Iceland
270 and, more generally, in HLD sources. The major focus is to understand the geological controls for
271 sediment accumulation, while characterizing the mineralogical composition, PSD, mode of occurrence
272 of Fe, degree of cohesion and VNIR reflectance spectra of the dust-emitting sediments in the Jokulsá
273 á fjöllum basin from Vatnajökull (front of the glacier) to Holuhraun (lava field in the middle of the

Eliminado: distinct

Eliminado: HLD

276 basin) and towards the sea (Figure 1). As a result, a conceptual model for the accumulation of fine-
 277 grained sediments and dust emission in the region is elaborated. Additionally, the analysis of samples
 278 from other prominent Icelandic dust sources, including Dyngjuvatn, Hagavatn, Landeyjasandur,
 279 Mælifellsandur, Mýrdalssandur and Skaftarsandur (Figure 1), are used to evaluate to what extent
 280 sediment properties differ across Icelandic dust-hotspots. Finally, the properties of Iceland's dust
 281 emitting-sediments are compared with those from a hotspot recently analysed with the same
 282 techniques in the Moroccan Sahara (González-Romero et al., 2023).

283 2. Methodology

284 2.1 FRAGMENT field campaigns

285 This study is part of the FRontiers in dust minerAloGical coMposition and its Effects upoN climaTe
 286 (FRAGMENT) project, which has conducted a series of coordinated and interdisciplinary field
 287 campaigns across remote dust sources. The project aims to enhance understanding and quantification
 288 of dust-source properties and their relationship with emitted dust characteristics, evaluate and refine
 289 ongoing spaceborne spectroscopy retrievals of surface minerals (Green et al., 2020), and improve the
 290 representation of dust mineralogy in Earth system models (Perwitz et al., 2015; Li et al., 2021;
 291 Gonçalves et al., 2023; Oviso et al., 2023). FRAGMENT campaigns entail regional sediment sampling
 292 along side intensive wind erosion and dust emission measurements at selected sites. Notable examples
 293 of these activities can be found in studies by González-Romero et al. (2023), González-Flórez et al.
 294 (2023), Panta et al. (2023), and Gonzalez-Romero et al. (2024). FRAGMENT campaigns have been
 295 executed in diverse geographic locations, including Morocco (2019), Iceland (2021), the United States
 296 (2022), and Jordan (2022).

297 This study presents results from the sediment sampling carried out from August 9 to September 10,
 298 2021 in Iceland. Sampling in the Jokulsá á Fjöllum basin, encompassing Dyngjusandur, took place
 299 between August 10 and 12, while samples from other dust emission hotspots across Iceland were
 300 collected throughout the extended period. The intensive field campaign on wind erosion and dust
 301 emission took place in Dyngjusandur (64°54'55"N 16°46'35"W), situated 300 m upstream from the
 302 newest sections of the Holuhraun lava field, where water can accumulate after flash floods, forming
 303 an endorheic lake. While some measurements from the intensive field campaign are used in this study
 304 to support the sediment sampling analysis in Dyngjusandur, the detailed results concerning the
 305 emitted (airborne) dust PSD, composition, and optical properties are presented in forthcoming
 306 companion studies (see e.g., González-Flórez et al., 2023, for preliminary findings), following the
 307 approach of previous FRAGMENT campaigns.

308 2.2 Sediment sampling across Iceland

309 In northern Iceland, within the Jokulsá á Fjöllum basin, Dyngjusandur stands out as the largest and
 310 most active dust-emitting area, as reported by Arnalds et al. (2010) (Figure 1). Originating from the
 311 Vatnajökull glacier, sand, silt and clay size particles are transported northwards via the Jökulsá á
 312 Fjöllum river and its tributaries such as as Kreppa, Arnardalsá and Skardsá, eventually reaching the sea
 313 (Figure 1). The Bárðarbunga eruption and subsequent formation of the Holuhraun lava field (from July
 314 29, 2014, to February 27, 2015 covering an area of 85 km²; Geiger et al., 2016) resulted in a natural

- Eliminado: . FRAGMENT
- Eliminado: performed
- Eliminado: t
- Eliminado: over
- Eliminado: in Morocco (2019), Iceland (2021), United States (2022) and Jordan (2022).
- Eliminado: better
- Eliminado: y
- Eliminado: the properties of dust-source sediments
- Eliminado: to the properties of the
- Eliminado: improve
- Eliminado: Earth system model
- Eliminado: The
- Eliminado: in Morocco, Iceland and Jordan included detailed...
- Eliminado: with an
- Eliminado: intensive
- Eliminado: campaign
- Eliminado: in one location
- Eliminado: (e.g., in Morocco, see
- Eliminado: ,
- Eliminado: o
- Eliminado: ,
- Eliminado: ;
- Eliminado: ,
- Eliminado: ; Yus-Díez et al., in prep/in submission 2023
- Eliminado: The FRAGMENT campaign in the US included sediment sampling only.
- Eliminado: reports the
- Eliminado: the
- Eliminado: basin
- Eliminado: and
- Eliminado: in
- Eliminado: Study site
- Eliminado: in
- Eliminado: has been reported
- Eliminado: The glacier
- Eliminado: is the source of
- Eliminado: that
- Eliminado: through
- Eliminado: to

356 dam that intercepted the basin's flow approximately 16 km downstream from Vatnajökull, leading to
357 the formation of the ephemeral Dyngjusandurvavn lake (referred to in this study as Dyngjusandur).
358 This area experiences recurrent flooding events every summer (Figure 1). The ponded waters
359 percolate through the Holuhraun lava field, eventually reconnecting again with the Jokulsá á Fjöllum
360 river downstream (Arnalds et al., 2016), facilitating the deposition of fresh sediments at Dyngjusandur,
361 which emits dust under favourable conditions.

362
363 Sediment samples were collected along the river to characterise the variability in particle size and
364 composition of sediments from the Vatnajökull moraine itself (front moraine) down to the sea (Jokulsá
365 á Fjöllum basin). This exhaustive sampling aimed to provide a comprehensive characterization of
366 sediments from this dust emission hotspot, located in the vicinity of the Dyngjusandur lake, prior to
367 encountering the Holuhraun lava field (Figure 1).

368
369 Moreover, sediment samples from other dust-emitting sources across Iceland were collected. These
370 include Dyngjuvatn (an endorheic lake near the Jökulsá á Fjöllum basin, but not directly connected to
371 it and distinct from Dyngjusandur), Hagavatn (an ephemeral lake where sediments pond, sediment
372 and sort), Skaftarsandur (riverine sediments near the coastline), Landeyjarsandur (riverine sediments
373 that flow towards the ocean and depositing), Mælifellsandur (river surrounding the glacier
374 contributing with fresh sediment), and Mýrdalsandur (riverine sediments on a wide riverbed) (Figure
375 1).

376
377 The collected samples represent surfaces typically found in dust-emitting and sandy areas across
378 Iceland. These samples comprise the top 1 cm (referred to as top sediment in this study) of recently
379 deposited sediments, typically within a few days of flooding events, originating from dust-emission
380 hotspots. Additionally, samples include underlying sediments located 1 to 5 cm beneath the surface
381 (referred to as fluvial sediments in this study), as well as aeolian ripples found in proximity of these
382 hotspots (Figure 2). Sampling was conducted using a metallic shovel, consistent with the approach
383 described in González-Romero et al. (2023), with a sampling area of 5 cm² and a height of 2 cm.
384 Detailed records, including coordinates, photographs of the locations and sampled area, and sample
385 characteristics, were documented. Subsequently, samples were stored in plastic bags and transported
386 to the laboratory. Upon arrival at the laboratory, samples were dried for 24-48 h at 50 °C and riffled
387 into smaller, equal, and homogeneous sub-samples for further treatment and analysis. A total of 119
388 samples were collected, of which 45 were selected for comprehensive analysis (29 top sediments, 8
389 fluvial sediments and 8 aeolian ripples). The remaining samples were subjected to XRD and particle
390 size distribution analysis, although the Fe mode of occurrence was not analysed in these samples.

391 2.3 Meteorology and airborne dust measurements in Dyngjusandur

392 As part of the intensive wind erosion and dust emission field campaign in Dyngjusandur, a variety of
393 instruments were deployed, following a setup similar to that utilized in Morocco (González-Flórez et
394 al., 2023). The measurement site was situated 300 m upstream from the newest sections of the
395 Holuhraun lava field, where water can accumulate after flash floods, forming an endorheic lake. For
396 this specific study, we relied on a reduced set of measurements including temperature, winds, soil
397 humidity and airborne dust concentration to describe the daily cycles of glacier melting, flooding,
398 sediment discharge and dust emission in Dyngjusandur.

Eliminado: e

Eliminado: away

Eliminado: forming

Eliminado: , which is affected by

Eliminado: recurrently

Eliminado: are filtered through

Eliminado: after the lava field

Eliminado: and allows the

Eliminado: can

Eliminado: of the

Eliminado: , with an

Eliminado: that

Eliminado: better

Eliminado: characterise

Eliminado: -

Eliminado: the surroundings of

Eliminado: before

Eliminado: Furthermore

Eliminado: sediments

Eliminado: in different hotspot sources around Iceland,

Eliminado: ing

Eliminado: not to be confused with

Eliminado: sea coast

Eliminado: a

Eliminado: that

Eliminado: s

Eliminado: and

Eliminado: es

Eliminado: z

Eliminado: d

Eliminado: present

430 The dust concentration and PSD were derived from a Fidas 200S (Palas GmbH) optical particle counter
431 placed at ~2m height. We recorded 1-s average number concentrations of suspended dust across 65
432 diameter size bins of equal logarithmic width, ranging from 0.39 to 42.17 μm, which were
433 subsequently averaged over 15 min intervals and converted to mass concentration for analysis. Data
434 from the first three bins were disregarded due to an unrealistic abrupt decline in concentration,
435 stemming from measurement limitations at the lower end of the size spectrum. Therefore, for
436 analytical purposes we deemed the Fidas instrument effective from the fourth bin, starting at 0.49 μm,
437 onwards.

438 Additionally, a second Fidas instrument was positioned at a higher elevation, enabling the
439 determination of the diffusive dust flux following the methodology outlined in González-Flórez et al.
440 (2023). For the purposes of this study, the obtained diffusive dust flux was solely employed to identify
441 all 15-min periods characterized by dust emission, indicated by positive diffusive dust flux in all size
442 bins between 0.65 μm and 27.38 μm. These dust emission periods were used to calculate the average
443 mass median diameter of the surface concentration of freshly emitted dust. A forthcoming companion
444 paper will provide a detailed analysis of the diffusive flux PSD during the campaign.

445 Both Fidas underwent calibration in the field at the onset of the campaign, utilizing monodisperse
446 (non-absorbing) polystyrene latex spheres (PSLs). Consequently, the default optical diameters
447 correspond to PSLs that produce the same scattered light intensity as the measured dust particles.

448 Measurements with the Fidas instruments started on August 11, 2021, at 17:30 UTC and continued
449 until September 4 at 11 UTC. Within this timeframe, we also used 15-min averaged wind data from
450 five 2-D sonic anemometers (Campbell Scientific WINDSONIC4-L) positioned at heights of 0.4, 0.8, 2,
451 5, and 9.9 m in a 10-m meteorological tower. Additionally, we used temperature from a probe
452 (Campbell Scientific HC2A-S3) installed near the tower at a height of 0.5 m, and from three soil water
453 content reflectometers (Campbell Scientific CS616). Two of these reflectometers were positioned
454 horizontally at depths of approximately 2 cm (referred to as VWC1) and 5 cm (referred to as VWC2),
455 respectively. The third reflectometer was positioned vertically at a depth of approximately 30 cm
456 (referred to as VWC3).

457 The Fidas instruments underwent temporarily dismantling from August 24 at 18 UTC to August 27 at
458 12 UTC due a significant flooding event at our measurement site, prompting concerns about potential
459 instrument damage. Additionally, throughout the campaign, minor data gaps occurred due to power
460 failures and other technical issues. The temperature probe and the soil water reflectometers were
461 also dismantled on the morning after the flooding. They were subsequently reinstalled on August 27
462 at 13 UTC and August 28 at 12:45UTC, respectively, to resume data collection.
463

Eliminado: to

Eliminado:

Eliminado: ,

Eliminado: f

Eliminado: ,

469 In addition, throughout the campaign, images of our measurement
470 site were recorded by a Raspberry Pi 3B+ (Raspberry Pi Ltd.,
471 Cambridge, UK) using a Webcam with a OV5647 camera module
472 (OmniVision, Santa Clara, CA, USA) with a 160 degree diagonal fisheye
473 lens attached. The image resolution is 2592 x 1944 pixels. The camera
474 was positioned to capture the upward view of the floodplain facing
475 the direction of the incoming water from the glacier (Figure S1).
476 Images were taken at intervals of every 15 minutes from August 8 at
477 18 UTC to August 25 at 13:30 UTC, and subsequently at intervals of
478 every 5 minutes until Sep 5 at 16 UTC. The images were manually inspected for rain
479 or flooding occurrence. Typically, this inspection was feasible during daytime hours (approximately
480 from 4 UTC to 22 UTC) depending on lighting conditions. However, for some nights, information was
481 available due to illumination from full moonlight. The following conditions were classified based on
482 the images: 'rain at site' was identified by falling droplets visible in the image or droplets present on
483 the camera housing, which changed from image to image; 'flooding visible in distance' was identified
484 by filled water channels or ponding water visible in the image; 'flooding at site' was identified when a
485 water surface stretched towards the bottom of the image and apparently beyond (the lower image
486 edge shows the ground in approx. 1 m distance of the camera) (Figure S1). **2.4 Analyses of sediment**
487 **samples**

488 2.4.1 Particle size distribution

489
490 Particle size distributions (PSDs) were analysed through fully dispersed (natural aggregates totally
491 dispersed, as much as possible through a dispersion shaking) and minimally dispersed methods
492 (natural aggregates minimally dispersed, dry measurements) according to González-Romero et al.
493 (2023). A coarser minimally dispersed PSD indicates high aggregation, while similarity between the
494 minimally and totally dispersed PSDs indicates a low aggregation of particles in dust-emitting
495 sediments; this has key implications for the mechanisms of dust emission. In both cases, PSDs were
496 determined by laser diffraction with a Malvern Mastersizer 2000 Scirocco and a Hydro G accessories,
497 for minimally and fully dispersed conditions, respectively. For the fully dispersed conditions, we
498 followed the procedure presented in Sperazza et al. (2004).

499 2.4.2 Mineralogical composition

500
501 X-Ray Diffraction (XRD), coupled with the Rietveld method, has been increasingly used as a fast and
502 reliable method to evaluate the content of the crystalline and amorphous phases in inorganic
503 materials (Rietveld, 1969; Cheary and Coelho, 1992; Young, 1993 and Topas, 2018). Quantification of
504 mixtures via the Rietveld method is generally restricted to crystalline phases for which structures are
505 well known. However, the addition of a known amount of an internal standard material allows the
506 quantification of any amorphous (non-crystalline) material in the mixture that has not been included

Eliminado:

Eliminado:

Eliminado: ,

Eliminado: ,

Eliminado: ¶

Eliminado: is

Eliminado:

Eliminado: ¶

Eliminado: 4

Eliminado: 4

Eliminado: would

Eliminado: would indicate

Eliminado: in

Eliminado: totally

Eliminado: 4

522 in the model, in our case, volcanic glass or amorphous alteration products like allophane, imogolite
523 and silica (De la Torre et al., 2001; Madsen, 2001, Scarlett and Madsen, 2006; Machiels et al., 2010;
524 Ibañez et al., 2013). Sample preparation for quantitative mineralogical analysis consisted of
525 preliminary dry grinding of the samples in an agate mortar, mixed with a known amount (10-20 %) of
526 CaF₂ powder (Merck), as an internal standard to allow the determination of amorphous contents, and
527 finally dry grounded again to reduce the grain size distribution and homogenise the mixture. The
528 analysis was carried out by a Bruker D8 A25 Advance powder X-ray diffractometer equipped with a
529 LynxEye 1D position sensitive detector, monochromatic Cu K α radiation ($\lambda = 1,5405 \text{ \AA}$) operating at 40
530 kV and 40 mA. The diffractograms were recorded by scanning from 4° to 120° of 2 θ with a step size
531 of 0.015° and a counting time of 1s/step maintaining the sample in rotation (15/min). The mineral
532 identification was performed by searches and comparisons of the patterns from International Centre
533 for Diffraction Database (ICDD, PDF-2) using DIFFRAC.EVA software package (Bruker AXS). The
534 quantitative analysis of the mineral phases was carried out by Rietveld full-pattern analyses performed
535 with the TOPAS 5 software (Bruker AXS), which uses least-square procedures to minimise the
536 differences between the observed and calculated diffractograms. The abundances of the crystalline
537 and amorphous phases were normalised to 100 %wt (weight percentage). The quality of the fitting
538 was evaluated by visually comparing the observed and calculated diffractograms to achieve a realistic
539 model and checking the residual factors (R_b , R_{wp} , R_{exp}) and goodness of fit (GOF) calculated by the
540 TOPAS model (Rietveld, 1969; Toby, 2006).

541 2.4.3 Mode of occurrence of Fe

542 The samples were subject to a series of sequential extractions (Figure S2) aimed at quantifying the
543 content of Fe, including readily exchangeable Fe, hematite and goethite, magnetite, as well as, Fe
544 bearing minerals and volcanic glass. Initially, a portion of each collected sample was subject to
545 duplicate acid digestion using a specialised two-step acid digestion method (Figure S2a) (Querol et al.
546 1993, 1997). This process was employed to ascertain the total Fe content. To validate the accuracy of
547 the analytical and digestion methods, reagent blanks and the standard reference materials NIST SRM
548 1633b (FA) were also subject to digestion. The determination of readily exchangeable Fe ions and
549 nano Fe-oxides, the quantification of crystalline Fe-oxides as hematite and goethite, and the
550 assessment of crystalline magnetite, were all conducted using the laboratory-based sequential
551 extraction method described by Shi et al. (2009) and Baldo et al. (2020). The initial sequential
552 extraction step involved combining 30 mg of the sample with 10 ml of the first extractant solution
553 (ascorbate solution as described in Figure S2b). The mixture was agitated for a period of 24 hours in a
554 light-controlled environment and subsequently filtered. Following this, another 30 mg of the same
555 samples underwent leaching with 10 ml of the second extraction solution (dithionite solution as
556 described in Figure S2c), with 2 hours of shaking under in a light-controlled environment, followed by
557 filtration. The solid residue resulting from this latter extraction was once again leached in a light-
558 controlled environment, this time using 10 ml of a third extraction solution (oxalate solution as
559 described in Figure S2d) and was shaken for a duration of 6 hours before undergoing another filtration.
560 The quantification of the dissolved Fe in each of the three solutions, as well as the bulk acidic digestion,
561 was performed using Inductively Coupled Plasma Atomic Emission Spectrometry (ICP-AES).

562 The bulk Fe content is referred to as FeT. The Fe that is the extractable from the initial leaching process
563 is denoted as FeA, representing the Fe that is readily exchangeable, as well as the Fe present as nano

Eliminado: 4

Eliminado: ed

Eliminado: 1

Eliminado: 1

Eliminado: S1b

Eliminado: S1c

Eliminado: S1d

571 Fe-oxides. The Fe extracted from the second stage, minus FeA, is referred to as FeD, which
572 corresponds to the Fe content of goethite and hematite. Additionally, the Fe content of the third
573 extraction is referred to as FeM, equivalent to the Fe magnetite content. The sum of FeD and FeM
574 is equivalent to the total Fe present in crystalline Fe-oxides. Finally, the FeT minus the sum of FeA, FeD,
575 and FeM is designated as FeS, representing the content of structural Fe or Fe incorporated within the
576 structure of other minerals, such as pyroxenes, other Fe-bearing minerals, and volcanic glass.

577 For quality control purposes in each laboratory-based sequential extraction, 30 mg of the Arizona Test
578 Dust (ATD; ISO 12103-1, A1 Ultrafine Test Dust; Powder Technology Inc.) was subject to the same
579 extraction procedure. The averaged Fe content of the reference material 1633b was found to be
580 7.6±0.5 % (certified 7.8 %). Furthermore, the average values of the sequential Fe extraction of the ATD
581 reference material were 0.062±0.005, 0.45±0.01, and 0.042±0.002 % for FeA, FeA+FeD and FeM,
582 respectively, while the certified contents are 0.067, 0.48, and 0.047 %, respectively.

583 2.4.4 [Electron microscopy of samples](#)

584 Particles from sediment samples were deposited on graphite stubs and sputter coated with C for size,
585 morphology, mineralogy, and aggregate evaluation analysis with a JEOM JSM-7001F SEM-EDX
586 Scanning Electron Microscope (SEM).

587 2.5. [In-situ and airborne VNIR spectroscopy](#)

588 Reflectance spectra were measured at 17 sampling locations before and after sample collection using
589 an ASD Fieldspec 3 with contact probe attachment. This instrument measures wavelengths 350-2500
590 nm with spectral resolutions of 3 nm at 0.7 µm and 10 nm at 1.4 and 2.1 µm. Spectra are measured at
591 1.4 nm sampling for wavelengths 0.35-1.0 µm and 2 nm for 1.0-2.5 µm but are internally resampled
592 and output with 1 nm spacing. All measurements are relative to Spectralon and corrected for the
593 known reflectance properties of Spectralon. While we measured the [exposed surface](#) after sampling
594 ([below the collected sample](#)), we did not use those measurements as the soils were too saturated to
595 see the mineralogy well. Surface spectra are reported and compared with spectral libraries and the
596 literature (e.g., Kokaly et al., 2017), and band depths (Table S1) were calculated for key absorption
597 features following the methods of Clark and Roush (1984).

598 Additionally, airborne imaging spectrometer (AVIRIS) data operated by NASA/JPL was acquired at the
599 Jokulsá á Fjöllum basin, from the glacier down to Holuhraun lava field during the field campaign. Three
600 AVIRIS scenes with 224 contiguous channels of 10 nm and a wavelength range of 0.35-2.5 µm were
601 used to map spectral reflectance characteristics with the expert Tetracorder system (a modified
602 absorption band-shaped comparison technique between obtained data and a library reference
603 spectrum, Clark et al. 2003). The AVIRIS raw data were calibrated to radiance, ratioed to the solar
604 spectrum and the atmospheric scattering and absorptions were removed to derive apparent surface
605 reflectance (Thompson et al. 2019 and or Brodrick et al. 2021). The AVIRIS reflectance image cubes
606 were mapped with [Tetracorder](#), which analyzed the spectra for hundreds of minerals, mineral
607 mixtures, coatings, vegetation, man-made materials and other compounds. Tetracorder analyses
608 different spectral regions for different compounds. While some minerals have unique spectral
609 features (e.g., hematite, pyroxene), others have broadly-overlapping absorption features and only
610 categories can be determined, e.g., Fe²⁺ bearing mineral.

Eliminado: 4

Eliminado: Scanning electron microscopy

Eliminado: 5

Eliminado: subsurface

Eliminado: , 2023

Eliminado: t

617 **3. Results and discussion**

618 **3.1 Glacier melting, flooding, sediment discharge and dust emission cycles in Dyngjúsandur**

619 Strong winds in Iceland typically coincide with extratropical cyclones featuring robust precipitating
620 systems, commonly known as fronts. During such weather events, dry conditions prevail on the
621 downstream side of Iceland's central highlands, providing favorable conditions for dust emission
622 (Dagsson-Waldhauserova et al., 2014). Wind patterns vary monthly, with the windiest months in
623 Northeast (NE) Iceland being May-June and September, correlating with high dust frequency. Dust
624 episodes in Dyngjúsandur are most commonly occurring during the warm season when the surface is
625 free of snow and glacier melting is accelerated, especially at midday. The plains cool rapidly during the
626 night, but they warm up fast in the sunshine of the long summer days, implying large daily fluctuations
627 in temperature and wind, the latter partly driven by katabatic winds from the Vatnajökull glacier
628 (Baratoux et al., 2011; Björnsson et al., 2017).

629 Figure 3 illustrates the time series of temperature, wind speeds, soil humidity, and near-surface dust
630 concentrations, along with the periods with 'rain on site', 'flooding visible in distance', and 'flooding
631 visible on site' at the measurement site. Typically, temperatures ranged between 5°C and 15°C (Figure
632 3a). However, only six days experienced temperatures exceeding 15°C, with the highest peak recorded
633 on August 24, when a new maximum temperature record for August was registered in Iceland
634 (<https://en.vedur.is/about-imo/news/the-weather-in-iceland-in-2021>). This temperature surge
635 intensified the daily meltwater discharge cycle of the Vatnajökull glacier, resulting in complete
636 flooding of our measurement site. This event coincided with the peak of volumetric water content
637 recorded during this period (Figure 3c), with a significant amount of sediments transported and
638 deposited by the glacial meltwater. Subsequent days were marked by vigorous winds, with 15-minute
639 average velocities at 9.9 m height exceeding 18 m/s (Figure 3b), and gusts reaching speeds beyond 25
640 m/s. These windy conditions led to a fast drying of the surface and intense dust storms, with persistent
641 dust concentrations exceeding 10000 µg/m³ (Figure 3d). The strong winds exposed the horizontal
642 reflectometers, necessitating multiple reinstallation attempts to maintain adequate coverage.
643 Consequently, the reliability of measurements from sensors VWC1 and VWC2 declined after the
644 flooding event, reflected in their representation as dotted lines in Figure 3c.

645 Before the significant flooding event, winds were weaker (Figure 3b), rain was frequent (vertical green
646 lines in Figure 3c), and milder flooding events were visible in our camera recurrently during the
647 afternoon (vertical blue lines in Figure 3c), the latter particularly before August 17. (Flooding events
648 between the moraine and the measurement site occurred daily, although our camera could only
649 capture those reaching areas near the measurement site.) Dust events during this period were
650 shorter-lived and less severe, with background concentrations around 1 µg/m³ (Figure 3d). The
651 volumetric soil water content tended to decrease, and its diurnal variations were more pronounced
652 near the surface (VWC1 and VWC2), with peak values typically occurring in the early morning and
653 decreasing throughout the afternoon due to evaporation. The periods of identified flooding,
654 particularly those with flooding visible on site (vertical dark blue lines in Figure 3c), or rain (vertical
655 green lines in Figure 3c) were clearly reflected in abrupt increases in volumetric water content. **3.2**

656 **Sediment particle size distribution**

Con formato: Justificado

Eliminado: ¶

Eliminado: 1

Eliminado: P

660 The PSD of the sediments collected were analysed and the obtained minimally dispersed particle size
661 distributions (MDPSD, i.e., near-natural aggregation state) and fully dispersed particle size
662 distributions (FDPSD, i.e., aggregates completely dispersed) were compared to evaluate the state of
663 particle aggregation in dust-emitting sediments.

664 3.2.1 Particle size distribution in the Jökulsá á Fjöllum basin both the MDPSD and FDPSD of the three
665 types of sediments (top surface, fluvial and aeolian ripples) are characterised by left-skewed log-
666 normal PSDs. PSDs of top sediments, fluvial sediments and aeolian ripples differ considerably, with an
667 increasingly coarser PSD (Figure 4). The mean of the median diameters (mean median diameters) from
668 the FDPSDs of all samples types collected in the basin was $133\pm 174\ \mu\text{m}$ [6.8,738, minimum and
669 maximum], while that of MDPSDs reached $107\pm 129\ \mu\text{m}$ [6.4,502], indicating the variability of particle
670 sizes. FDPSDs of top sediments had a much finer mean median diameter ($31\pm 15\ \mu\text{m}$) compared to the
671 other type of samples: 102 ± 91 and $354\pm 203\ \mu\text{m}$ for fluvial sediments and aeolian ripples, respectively
672 (Table 1). Similar results, in absolute and relative values, were obtained for MDPSDs for all types of
673 samples (Table 1). The fact that FDPSD and MDPSD yielded similar mean median diameters indicate a
674 significant level of particle disaggregation, which is unusual for dust-emitting sediments in hot deserts
675 (González-Romero et al., 2023).

676 The mean median diameter of top sediments along the basin, ranging from the glacier to the sea,
677 clearly decreases, first transitioning from $76\ \mu\text{m}$ for FDPSD and $52\ \mu\text{m}$ for MDPSD near the moraine,
678 to $19\ \mu\text{m}$ for FDPSD and MDPSD just before the Holuhraun lava field (Figure 5). Notably, just before
679 the Holuhraun lava field, where the intensive measurements were conducted, the mass median
680 diameter the dust concentration during dust events averaged $\sim 12\ \mu\text{m}$ between 0.5 and $40\ \mu\text{m}$. For
681 reference, the mean mass diameter of the MDPSD and FDPSD of the top sediments around the
682 measurement site within the same size range is $\sim 15\ \mu\text{m}$.

683 The reduction in the median diameter of the top sediments along the path from the glacier to the lava
684 field occurs due to several factors. On the one hand, there is particle size segregation driven by fluvial
685 transport that carries sediment from the moraine to more distant areas. On the other hand, vertical
686 micro-segregation occurs during deposition at the ephemeral lake formed by the Holuhraun lava field,
687 which effectively acts as a natural dam. Because of this dam-like effect, sediment-laden waters are
688 temporarily impounded. Finer-grained top sediments gradually accumulate on top of the coarser
689 sediment layer deposited during the initial stage of the flooding-ponding-drying cycle. As shown in
690 Section 3.1, these episodic events are recurrent during the summer season.

691 The fine pattern of these surface sediments likely stems from various factors: i) sediments trapped
692 within glacial ice from fine volcanic ash deposits accumulated over the glacier's geological history,
693 along with nearby dust emissions that are released during melting; ii) the transportation of fine
694 sediments from moraines to floodplains via fluvial channels, where further segregation occurs through
695 ponding. During drying phases, finer particles settle atop, following the initial deposition of coarser
696 particles; iii) dust emissions contribute to segregating finer particles on rock surfaces, sediments, and
697 ice, which are then transported to floodplains during subsequent flooding or rain events. We term this
698 latter process as aeolian recycling of fine sediments.

699 Frequently, layers of former top sediments were buried beneath fluvial sediments. Flood events led
700 to the inundation of unpaved roads towards the moraine typically in the midday to late afternoon

Eliminado: 1

Eliminado: ¶

The PSD of the sediments collected were analysed and the obtained minimally dispersed particle size distributions (MDPSD, i.e., near-natural aggregation state) and fully dispersed particle size distributions (FDPSD, i.e., aggregates completely dispersed) were compared to evaluate the state of particle aggregation in dust-emitting sediments. Jökulsá á Fjöllum basin includes Dyngjúsandur (approximately 14 to 18 km away from the Vatnajökull glacier, see in detail in 3.1.2). ¶

Eliminado: B

Eliminado: 3

Eliminado: the Jökulsá á Fjöllum

Eliminado: high state

Eliminado: (

Eliminado:)

Eliminado: of top sediments

Eliminado: close to

Eliminado: down

Eliminado:

Eliminado: 4

722 hours. Conversely, when insolation and temperature markedly decreased, these flooding episodes
723 were reduced. Low wind speeds facilitated the preservation of surface sediments, which were
724 subsequently covered by flood deposits during days of minimal water flow, preventing erosion of the
725 now-buried top layers. During the sunny August days, a recurring cycle often ensued: midday to late
726 afternoon flooding followed by drying and dust emission the following day (Figure 3). However,
727 instances of reduced drying due to rain or diminished insolation inhibited dust emission on subsequent
728 days (Figure 3). Additionally, if flooding intensity peaked on a particular day, insufficient drying
729 prevented dust emission the following day.

730 After the Holuhraun lava field, the mean median diameter of top sediments increases again, peaking
731 at 47 μm for FDPD and 41 μm for MDPSD, owing to sediment input from tributary channels of the
732 Jökulsá river (Figure 5). The water accumulated in this natural dam gradually permeates through the
733 rocks and sediments and subsequently flows through the Holuhraun lava field. These processes lead
734 to sediment removal from the water. This filtered water continues its course until it connects with
735 tributary channels and the segment of the Jökulsá á Fjöllum river that encircles the lava field. At this
736 juncture, these sediment-laden channels merge with clearer waters originating from the lava field
737 post-filtration. Moreover, beyond the lava field, the channels are typically incised, and flooding events
738 are infrequent. The deepening of fluvial channels due to erosion renders the floodplains incapable of
739 inundation. Consequently, there are no floodplains with surface sediments available for sampling, and
740 the spatial prevalence of fine-grained top sediments along this stretch, on the way to the sea, is rare.
741 This reduction in fine sediment cover significantly diminishes the potential for dust emissions.
742 Subsequently, near the sea, the diameter decreases again, reaching 29 μm for FDPD and 27 μm for
743 MDPSD (Figure 5). There, sediment deposition leads to extensive mudflats adorned with top
744 sediments, where emission becomes more likely once again if conditions are favourable. For fluvial
745 sediments and ripples there are not enough samples, and the decreasing trend was not observed.

746 The analysis revealed consistent findings between MDPSD and FDPD for samples exhibiting relatively
747 fine mean median diameters. However, we note that the MDPSD showed finer particles than FDPD
748 in samples with finer mean diameters (Figure 5). This discrepancy is likely attributable to the presence
749 of pumice particles. Pumice, characterized by its fragility and low density, is common across Iceland,
750 forming layers several centimetres thick, as observed in Dyngjuvatn. These particles, with sizes ranging
751 from a few microns to approximately 65 μm , are buoyant in water and easily fragmented. This poses
752 a challenge during FDPD wet analysis, as these water-buoyant particles evade capture within the
753 measurement chamber, because a homogeneous particle dispersion is required. Consequently, FDPD
754 measurements tend to underestimate the presence of finer pumice particles, resulting in a coarser
755 PSD. Conversely, MDPSD measurements, conducted in dry conditions, circumvent this issue by
756 accurately detecting finer pumice particles. Thus, MDPSD yields a finer median diameter, reflecting
757 the inclusion of these smaller particles in the analysis.

758 Close to the moraine the energy of the fluvial system is so high that the pumice particles are
759 transported far from the ice thawing areas. When flooding occurs in the lowlands fluvial suspended
760 particles are deposited first and the buoyant pumice particles only when ponded waters percolate and
761 or dry. This leads to a segregation of pumice particles, with a progressive enrichment downstream of
762 the fluvial system and in ponded lowlands. Furthermore, these processes lead to an enrichment of
763 pumice in the surface of the ponded areas, and this favors dust emissions of fine and light particles.

Eliminado:

Eliminado: the

Eliminado: to up to

Eliminado: due

Eliminado: 4

Eliminado: Once the water reaches

Eliminado: the sea,

Eliminado: yield

772 However, top sediments near the glacier are more consolidated because in this high-water energy
773 environment the outcrops of fine top sediment layers are the ones exposed by erosion of the old
774 sedimentary sequences composed of a conglomerate in the base, sandy sediments in the middle part
775 and fine ones in the top, but not from the recent flooding. These older top sediments are much more
776 consolidated and, as shown by Figure 5, the averaged mean diameters of the MDPSD are much coarser
777 than those of the FDPSP.

Eliminado: of layers

Eliminado: s

Eliminado: the one from

778 3.2.2 Particle size distribution at different Icelandic dust hotspots

Eliminado: 1

779 The median FDPSPs of top sediments found in most Iceland's dust-emitting regions (Dyngjusandur,
780 Skaftarsandur, Landeyjarsandur and Mælifellsandur) closely resemble the MDPSDs (Figure 6). This
781 underscores the limited degree of particle aggregation in these areas. However, in the cases of
782 Dyngjuvatn, Mýrdalssandur and Hagavatn the FDPSPs and MDPSDs of top sediments differ slightly
783 (Figure 6).

Eliminado: 5

Eliminado: 5

784 The mean median diameter of both the FDPSP and MDPSD for the 23 top sediments sampled across
785 Iceland is $56\pm 69\ \mu\text{m}$ [2.9,263, min., max.] and $55\pm 62\ \mu\text{m}$ [3.3,234], respectively. Notably, top
786 sediments from Mýrdalssandur and Dyngjuvatn exhibit coarser mean median diameters, measuring
787 147 ± 108 and $146\pm 156\ \mu\text{m}$ for FDPSP, and 163 ± 92 and $100\pm 105\ \mu\text{m}$ for MDPSD, respectively. These
788 diameters are more than two times coarser than the overall Iceland mean median diameter (Table 1).
789 Conversely, Skaftarsandur, Mælifellsandur and Landeyjarsandur show mean median diameters that
790 are similar those of the average top sediments in Iceland (Table 1). On the other hand, the top
791 sediments from Dyngjusandur and Hagavatn (the largest dust hotspots associated with ephemeral
792 lakes) exhibit the finest mean median diameters, specifically 24 ± 15 and $16\pm 12\ \mu\text{m}$ for FDPSP, and
793 24 ± 1 and $26\pm 26\ \mu\text{m}$ for MDPSD, respectively. These diameters are approximately two times finer than
794 the average of top sediments in Iceland (Table 1).

Eliminado: 2

Eliminado: 2

Eliminado: 2

795 Our results show a general lack of cohesion in the dust-emitting top sediments of Iceland sources, as
796 evidenced by the similar FDPSP and MDPSD results. As discussed in Section 4 and 5, this suggests that
797 in addition to saltation, aerodynamic entrainment of dust without saltation as an intermediate process
798 is likely a complementary dust emission process in Iceland due to reduced cohesive forces.

Eliminado: strongly

799 3.3. Mineralogy

Eliminado: 2

800 3.3.1 Mineralogy of sediments at the Jökulsá á Fjöllum basin

Eliminado: 2

801 Different sediments and locations of the Jökulsá á Fjöllum basin were analysed to describe the
802 variability in the region and therefore explain probable mineralogic fingerprints important for dust
803 emission models. The results show that amorphous phase is the prevailing component of the samples
804 analysed ($79\pm 11\ \text{wt}\%$), being most probably volcanic glass and its nano sized weathering product
805 (hydrated amorphous Si-bearing). Also showed anorthite ($11\pm 6.6\ \%$, a Ca-plagioclase, $[\text{Ca}_{0.95-1}\text{Na}_{0.05-0}]$
806 $\text{Al}_2\text{Si}_2\text{O}_8$), augite ($7.7\pm 5.4\ \%$, a pyroxene, $[\text{Ca}_x\text{Mg}_y\text{Fe}_z][\text{Mg}_{y1}\text{Fe}_{z1}]\text{Si}_2\text{O}_6$), andesine ($1.7\pm 5.9\ \%$, a
807 plagioclase, $[\text{Na}_{0.5-0.7}\text{Ca}_{0.5-0.3}]\text{Al}_2\text{Si}_2\text{O}_8$), analcime ($0.19\pm 0.36\ \%$, a Na-zeolite probably formed from the
808 devitrification of volcanic glass during weathering, $\text{Na}[\text{AlSi}_2\text{O}_6]\cdot\text{H}_2\text{O}$), magnetite ($<0.5\ \%$, Fe_2O_4) and Ca-
809 mordenite ($<0.1\ \%$, a Ca-zeolite, $\text{Ca}_4[\text{Al}_8\text{Si}_4\text{O}_{96}]\cdot 28\text{H}_2\text{O}$) (Figure 7, Table S2).

Eliminado: '

Eliminado: 6

824 The average composition of the top sediment samples comprises approximately 75±12 % volcanic
825 glass, 11±7.4 % anorthite, 9.9±6.4 % augite, 3.6±8.1 % andesine, along with trace amounts of
826 0.26±0.40 % analcime, 0.16±0.34 % Ca-mordenite, and <0.5 % magnetite. Fluvial sediments and
827 aeolian ripples have similar (or slightly higher) content of amorphous phases (80±12 and 86±4.7 %,
828 respectively), augite (6.6±4.0 and 4.8±1.7 %), and magnetite (<0.5 and <0.5 %). Anorthite is enriched
829 in fluvial sediments and aeolian ripples compared to top sediments (13±7.7 and 9.6±2.9 %,
830 respectively) and also analcime for the underlying fluvial sediments (0.23±0.43 %), with andesine and
831 Ca-mordenite contents being below the XRD detection limits in both the underlying fluvial sediments
832 and aeolian ripples (Figure 7, Table S2). The slight enrichment of fluvial sediments and aeolian ripples
833 in amorphous phases and the slight depletion in augite is likely due to the coarser particle size and the
834 prevalence of relatively large particles of high glass basalt with fine inclusions of crystalline minerals.
835 As these coarser particles break down into finer particles the occurrence of particles made of the
836 crystalline inclusions might increase. Thus, the finer top sediments might be slightly enriched in these
837 crystalline fine minerals (and slightly depleted in glass) in comparison to the coarser underlying fluvial
838 sediments and aeolian ripples.

Eliminado: 6

839 The mineral composition of fluvial sediments is very homogeneous across the Jökulsá á Fjöllum basin;
840 however slight differences were observed for top sediment samples before and after the natural dam
841 of the Holuhraun lava field (Figure S3, Table S2). Before the natural dam, top sediments are enriched
842 in amorphous phases or volcanic glass relative to those between the Holuhraun lava field and the sea
843 (82±2.2 and 60±9.5 %, respectively). Furthermore, after the Holuhraun field, andesine, traces of Ca-
844 mordenite and hematite are detected (11±11, 0.48±0.46, and <0.5 %, respectively). For fluvial
845 sediments we observe similar trends with volcanic glass or amorphous phases enrichment before the
846 Holuhraun lava field (85±2.9 and 51±18 %) and minerals as andesine (16±18 %), forsterite (Mg₂SiO₄)
847 (2.8 %, 1 sample) and analcime (0.25 %, 1 sample) being detected only after the Holuhraun lava field
848 (Table S2). No trends were found for ripples due to a lack of samples after the Holuhraun lava field.
849 These differences are probably due to the different source areas for pre- and post- Holuhraun lava
850 field samples.

Eliminado: S2

851 Reflectance spectra of aeolian ripples (Figure 8a) have broad electronic transitions due to Fe²⁺ with a
852 minimum at ~1.05 µm. Most spectra also have an inflection indicating a second electronic transition
853 of Fe²⁺ at ~2 µm (e.g., Burns, 1993). These spectra also have vibrational absorption features, with
854 combination bands of H₂O at 1.91 µm and Si-OH and/or Al-OH at 2.2 µm (e.g., Clark et al., 1990).
855 Overall, spectra are consistent with volcanic glass (Bell et al., 1976; Horgan et al., 2014) with possible
856 minor contributions of pyroxene (e.g., Cloutis and Gaffey, 1993) and weak hydration, likely mostly
857 from a hydrated amorphous silica product such as hydrated basaltic glass, allophane, imogolite, or
858 opal (e.g., Anderson and Wickersheim, 1964; Goryniuk et al., 2004; Rampe et al., 2012).

Eliminado: 7a

859 Spectra of top sediments are more variable (Figure 8b). All have broad Fe²⁺ electronic transitions
860 centred at 1.00-1.05 µm likely due to volcanic glass and pyroxene, as in the aeolian ripples. Most lack
861 an electronic transition near 2.0 µm, although one sample from a floodplain appears to have a weak
862 feature. All spectra have H₂O combinations at 1.91 µm, and most have OH overtones at 1.41-1.44 µm
863 (e.g., Clark et al., 1990). Other than from a few places on the moraine, all top sediments spectra also
864 have narrower features at 2.20-2.22 µm, which are combination bands of Si-OH and/or Al-OH (e.g.,
865 Clark et al., 1990). One spectrum (#21) also has a weaker Fe(III)-OH combination band at 2.29 µm, seen

Eliminado: 7b

870 in hydroxylated Fe-bearing minerals such as Fe smectite clay or ferrihydrite (e.g., Bishop et al., 2008).
871 Spectra from three sites on the moraine have broader, deeper 1.4 and 1.9 μm features, indicating that
872 the soil was wetter.

873 AVIRIS imaging spectroscopy data from the glacier to Holuhraun lava field, show the presence of water
874 in the sediments (absorption features between 1 to 1.5 μm), with clinopyroxene presence (absorption
875 features at 2-micron band), olivine, and Fe^{2+} bearing minerals, some of which may be Fe^{2+} in the
876 volcanic glass. These results are aligned with mineralogy from XRD and in-situ reflectance spectra
877 (Figure 9). In the main study areas, at AVIRIS scale, there are only trace to small local outcrops of
878 minerals as hematite, goethite, calcite, dolomite, chlorite/serpentine, gypsum, illite, muscovite,
879 montmorillonite, and vermiculite (Green et al., 2020). Some trace calcite is seen in Figure 9 and local
880 outcrops of chlorite/serpentine. The strong signatures of Fe^{2+} bearing minerals in the dark soils and
881 rocks make it difficult to detect hematite and goethite unless the concentration is high enough for the
882 Fe^{3+} absorptions to be stronger than Fe^{2+} absorptions.

883 3.3.2 Mineralogy of sediments from different Icelandic dust-emitting hotspots

884 The average composition of the top sediments from the Iceland's dust-emitting hotspots is also
885 dominated by volcanic glass or amorphous phases ($68\pm 26\%$ wt), followed by anorthite, augite and
886 andesine (15 ± 11 and 8.6 ± 9.0 and $7.4\pm 19\%$), Fe-diopside ($1.4\pm 3.4\%$, a pyroxene with a $>50\%$ MgSiO_3
887 and 45-50% CaSiO_3 composition), and traces of quartz ($0.21\pm 0.47\%$), forsterite ($0.61\pm 1.7\%$), wairakite
888 ($0.19\pm 0.92\%$), analcime ($0.11\pm 0.28\%$), Ca-mordenite ($<0.1\%$), magnetite and hematite (<0.5 and <0.5
889 %) and pyrite (FeS_2 $<0.5\%$) (Figure 10, Table S3).

890 Volcanic glass or amorphous phases content is higher at Dyngjuvatn, where top sediments are
891 enriched in pumice, with a contribution of $89\pm 3.8\%$, followed by $82\pm 2.3\%$ at Dyngjusandur, $81\pm 2.8\%$
892 at Mælifellsandur, $75\pm 8.9\%$ at Mýrdalssandur, 68% (1 sample) at Skaftarsandur and $38\pm 3.9\%$ at
893 Landeyjarsandur (Figure 10, Table S3). At Hagavatn, however, the glass content reached only 13 ± 14
894 %, with the mineralogy being dominated by andesine ($53\pm 11\%$) and augite ($29\pm 3.8\%$), with minor
895 proportions of forsterite ($4.7\pm 1.3\%$), hematite ($<0.5\%$) and magnetite ($<0.5\%$) (Figure 10, Table S3).
896 Thus, in this case, the very high content of crystalline phases indicates a sediment originating from a
897 slowly cooled lava allowing a widespread crystallisation of minerals from the melt.

898 A very similar mineral composition was found among top sediments from Mælifellsandur,
899 Dyngjusandur, Skaftarsandur and Mýrdalssandur, where the main content was amorphous phases like
900 volcanic glass with some plagioclase and pyroxene species (Figure 10, Table S3). The highest content
901 of volcanic glass was found at Dyngjuvatn and the lowest content at Hagavatn. The occurrence of
902 magnetite was higher at Landeyjarsandur, Mælifellsandur and Mýrdalssandur, than in other dust-
903 emitting hotspots, according to XRD analysis. As seen in section (3.1.2), Hagavatn and Dyngjusandur's
904 top sediments have the smallest particle size, coinciding with the lowest volcanic glass content, in the
905 first case, but quite high in the second. Meanwhile Dyngjuvatn's (pumice-rich) top sediments have the
906 coarser particle size and the highest volcanic glass content. Mælifellsandur's and Mýrdalssandur's top
907 sediments have similar mineral composition, but those of Mýrdalssandur are coarser (near the river
908 mouth) in particle size compared to Mælifellsandur (upstream near the glacier). Landeyjarsandur's
909 top sediments are similar in particle size to the ones from Mælifellsandur, but with half of the volcanic
910 glass, and therefore with more plagioclase and pyroxene.

Eliminado: 8

Eliminado: 8

Eliminado: 2

Eliminado: 9

Eliminado: 9

Eliminado: 9

Eliminado: 9

918 Compared to Baldo et al. (2020), who analysed PM₁₀ mineralogy sampled in laboratory resuspension
919 of Icelandic sediments, samples for the current study are very similar for Hagavatn, Mælifellsandur
920 and Dyngjusandur, meanwhile for Landeyjarsandur and Mýrdalssandur the present results are lower
921 for volcanic glass and so, higher for pyroxene and plagioclase. Baratoux et al. (2011) found a similar
922 mineral composition of sediments from aeolian ripples at Dyngjusandur, with predominance of
923 volcanic glass (80-90 %). Moroni et al. (2018) found that the mineral composition of glaciofluvial
924 sediments was dominantly volcanic glass in Dyngjusandur, Mýrdalssandur and Mælifellsandur, with
925 lower proportions of plagioclase and pyroxene.

926 3.4 Mode of occurrence of Fe

927 3.4.1 Mode of occurrence of Fe at Jökulsá á Fjöllum basin

928 Iron speciation in dust-emitting sediments and surfaces control the amount of iron in the emitted dust
929 and therefore the effect in ocean and terrestrial ecosystems and climate. The average of FeT content
930 in the dust emitting sediments of the Jökulsá á Fjöllum basin is 9.5±0.40 %wt (Table S4). Top sediments
931 as well as underlying fluvial sediments and aeolian ripples exhibit similar average FeT contents with
932 values of 9.5±0.39 %, 9.5±0.43 %, and 9.4±0.41 %, respectively (Figure 11, Table S4). FeS, which
933 represents structural Fe found in volcanic glass and certain Fe-bearing crystalline species, constitutes
934 for the majority of FeT content, accounting for 80±6.3 %. This is, followed by smaller proportions of
935 FeM (magnetite) at 16±5.5 %, FeD (hematite/goethite) at 2.6±1.6 %, and FeA (readily exchangeable
936 Fe) at 1.2±0.40 % (Figure 11, Table S4). It is worth noting that these proportions are quite consistent
937 across top sediments, fluvial sediments and aeolian ripples, with FeS, FeM, FeD and FeA percentages
938 of 79±6.5 %, 16±5.4 %, 3.5±1.5 % and 1.3±0.39 % in the top sediments. In fluvial sediments, these
939 values are 82±8.7 %, 15±7.8 %, 2.2±1.4 % and 1.2±0.44 % and in aeolian ripples, they are 80±2.4 %,
940 18±2.4 %, 1.2±0.41 % and 0.85±0.22 % respectively (Figure 11, Table S4). Notably, there is a difference
941 in magnetite proportions between fluvial sediments from the pre-Holuhraun lava field and those from
942 the post-Holuhraun, with FeM accounting for 19±4.5 % and 11±1.3 % of total Fe, respectively. This
943 variation results in a reverse scenario for FeS, with percentages of 77±6.4 % and 84±1.9 %, respectively
944 (Figure 11, Table S4).

945 3.4.2 Mode of occurrence of Fe at different Icelandic dust-emitting hotspots

946
947 The content of FeT and proportions of FeS, FeA, FeD and FeM in sediments from Iceland's dust-
948 emitting hotspots are summarised in Table S5 and Figure 12.

949 The average FeT content in Iceland's top sediments is 9.3±1.5 %, with the highest concentrations
950 observed in Mælifellsandur and Mýrdalsandur, ranging from 10.0 % to 11.6 % wt, while the lowest are
951 found at Hagavatn and Dyngjuvatn, ranging from 5.5 % to 9.1 % wt. On average, FeS accounts for
952 79±5.4 % of the FeT, with minimum proportions of 65 % in one sample from Dyngjusandur and a
953 maximum of 89 % in one from Mælifellsandur. However, most samples are in the range of 75-80 %.

954 FeM constitutes 15±4.6 % of FeT, with minimum proportions of 7.2 % in one sample from
955 Landeyjarsandur and a maximum of 25 % in one from Dyngjusandur, but most samples fall within the
956 10-20 % range, with the highest proportions typically exceeding 20 % in Dyngjusandur. FeD accounts
957 for 5.0±3.1 % of FeT, with minimum proportions of 1.4 % in one sample from Dyngjusandur and a
958 maximum of 12 % in one from Hagavatn, but most samples fall within the 2-9 % range. FeA represents

Eliminado: 3

Eliminado: 3

Eliminado: 10

Eliminado: 10

Eliminado: 10

Eliminado: 10

Eliminado: 3

Eliminado: 11

967 only 1.6±0.74 % of FeT, with minimum proportions of 0.75 % in one sample from Dyngjusandur and a
968 maximum of 3.4 % in one from Hagavatn, but the majority of samples fall within the 1-2 % range.

969 The absolute contents of magnetite and hematite/goethite are quite low in the samples, making XRD
970 quantitative analysis uncertain. Consequently, the correlation with FeM and FeD is weak. This
971 highlights the importance of employing the chemical sequential extraction (Shi et al. 2009) to assess
972 the mode of occurrence of Fe and further constrain the mineral content of iron oxides. As mentioned
973 in previous sections (3.1.2 and 3.2.2), Dyngjusandur and Hagavatn have similar mean median particle
974 size, but different volcanic glass content. The content of FeS is similar between them, but in the other
975 hand, Hagavatn has higher proportions of FeA and FeD than FeM and Dyngjusandur more proportion
976 of FeM than FeA and FeD. Nevertheless, no correlation was found between mineralogy (from XRD)
977 and Fe speciation. **3.5 Spectroscopic indicators of mineral sorting**

978 Consistent with the PSD and mineralogical analyses, spectra acquired in situ of top sediments and
979 ripples also show systematic variations with distance from their source (Figure 13). Aeolian ripples,
980 composed of ~100 µm-sized grains weathered out of recent lava flows, were generally measured on
981 or near the lavas from which they are sourced and are coarser grained than top sediments. Thus, their
982 spectra are dominated by primary volcanic phases, including volcanic glass and pyroxene, with minor
983 alteration, either by magmatic fluids (hydrating the volcanic glass) or later alteration. Their spectra are
984 dark (low albedo), have weaker H₂O combination bands at 1.91 µm, and stronger Fe²⁺ electronic
985 transitions near 1 and 2 µm than most top sediments. Interestingly, the depth of the absorption
986 features around 2.21 µm is slightly stronger in these samples and most likely is from a hydrated
987 amorphous silica phase (Figure 13c). These samples unsurprisingly show no systematic trends with
988 distance from the glacier.

989 Top sediments, on the other hand, show stronger trends with distance from the glacier (Figure 13).
990 The albedo, measured as the mean from 1.62-1.63 µm, is brighter with increasing distance (Figure
991 13d). This may be due to a change in mineralogy from primary volcanic glass, olivine, and pyroxene to
992 brighter alteration products, including zeolites and phyllosilicate minerals, or due to decreasing
993 particle size, as volume scattering is enhanced with smaller grains. More likely, it is a combination of
994 both factors. With the exception of locations on the moraine that were wetter at the surface, the
995 depth of the absorption features due to H₂O at 1.91 µm increases with distance from the glacier
996 (Figure 13b). Conversely, the depth of the ≈1 µm Fe²⁺ electronic transition decreases (Figure 13a). As
997 discussed in Section 3.2.1, these variations are most likely the result of mechanical sorting, with finer
998 grained hydrated, altered phases becoming dominant downstream relative to coarser, unaltered
999 volcanic glass.

1000 The loss of volcanic glass and potentially amorphous hydrated silica within top sediments is also
1001 supported by closer examination of the spectra. In spectra of some top sediments, the ≈1.0 µm Fe²⁺
1002 electronic transition minimum shifts to slightly shorter wavelengths (≈1.03 µm in top sediments vs
1003 1.05 µm in ripples), and a secondary electronic feature at ≈1.2 µm is typically weaker or absent. These
1004 shifts are consistent with the proportion of pyroxene to volcanic glass increasing (Horgan et al., 2014).
1005 In addition, the ≈2.2 µm combination feature shifts from 2.22-2.25 µm in the ripples to 2.21 µm in
1006 some top sediment samples. The longer wavelength minima and broader features are more typical of

Eliminado: ¶

Eliminado: 4

Eliminado: 5

Eliminado: 12

Eliminado: feature

Eliminado: 12c

Eliminado: 12

Eliminado: 12d

Eliminado: feature

Eliminado: 12b

Eliminado: 12a

Eliminado: T

1019 hydrated amorphous silica (e.g., opal), whereas the shorter wavelength minima suggest the presence
1020 of a more ordered phase with Al-OH bonds.

1021 **3.6 Contrasts between Icelandic hotspots and a typical hot desert dust hotspot**

1022 Our findings reveal significant [differences](#) between sediments from the Moroccan Sahara (as
1023 described in Gonzalez-Romero et al., 2023) and those collected and analysed in Iceland. It is important
1024 to note that the Moroccan samples used for comparison were obtained from the Lower Drâa Valley,
1025 an arid inland drainage basin and a prominent dust hotspot, which is broadly representative of
1026 numerous crustal dust source areas in hot desert environments.

1027 The differences in sediment composition are closely intertwined with the particle size distribution and
1028 aggregation/cohesion characteristics of these sediments. For instance, when we examine the mean
1029 median diameters of the FDPD and MDPSD for top sediments collected from the lowlands and the
1030 ephemeral lakes of Iceland (Dyngjusandur), we observe a relatively close similarity in sizes (31 and 32
1031 μm , respectively) (as detailed in Table 1). In contrast, crusts from the lowlands in the Saharan source
1032 exhibit markedly different mean median diameters (7 and 131 μm , as reported by González-Romero
1033 et al., 2023) (Table 1). Therefore, the FDPD mean diameters for just crusts in the lowlands of the
1034 Saharan source are four times finer than those found in top sediments in Iceland. For the underlying
1035 fluvial sediments, we found that the MDPSD median diameters are 1.5 times coarser in the Saharan
1036 source in comparison to Iceland (115 and 74 μm , respectively). In contrast, for the FDPD the mean
1037 median diameter is finer in the Saharan source than in Iceland (22 and 102 μm , respectively).

1038 The resemblance between the FDPD and MDPSD of top sediments in Dyngjusandur, as well as the
1039 significant disparity with those from the Sahara, are attributed to the varying levels of aggregation and
1040 cohesion. These differences in aggregation are further substantiated by SEM observations (as shown
1041 in Figure 14a and b). They are likely a consequence of the paucity of cementing minerals in the Iceland
1042 top sediments, namely low levels of carbonate and sulphate content, as well as the absence of clay
1043 minerals. These factors contribute to the prevalence of dispersed and non-cohesive sediments in
1044 Iceland. The underlying fluvial sediments, which consist mainly of coarse particles, primarily individual
1045 granules derived from volcanic rock (as depicted in Figure 14c), also stands in contrast to the Sahara's
1046 dust-emitting sediments, which often exhibit particle aggregation. Notably distinct were Iceland's
1047 dust-emitting top sediments that showed a high enrichment of pumice, an exceedingly fragile and
1048 low-density volcanic rock, as seen in the Dyngjuvatn samples. In these cases, the particles often
1049 displayed elongated shapes and were accompanied by aggregation of finer particles (refer to Figure
1050 14d, e, and f). This distinctive characteristic led to a measurement artifact that resulted in unusually
1051 coarser FDPD readings compared to MDPSD.

1052 The lack of aggregation and cohesion of Icelandic dust-emitting sediments in comparison to the
1053 Saharan source strongly suggests that saltation in Iceland should be efficient, while at the same time
1054 dust could be emitted also by direct aerodynamic entrainment. Usually, dust emission due to
1055 aerodynamic entrainment is much less efficient than that generated by saltation bombardment,
1056 because interparticle cohesive forces, encompassing Van der Waals forces, electrodynamic forces, and
1057 chemical forces (e.g., Castellanos, 2005), increase on average with decreasing particle size. This results
1058 in an average minimum entrainment threshold for sand-size particles of around 70 - 100 μm (Shao
1059 and Lu, 2000; Shao and Klose, 2016). Toward smaller and larger particle sizes, increasing cohesive and

Eliminado: 4

Eliminado: .

Eliminado: in composition, particle size distribution, aggregation/cohesion and reflectance spectra

Eliminado: 3

Eliminado: 3

Eliminado: 13a

Eliminado: 13c

Eliminado: 13d

1069 gravitational forces, respectively, require stronger lifting forces for particle entrainment. However, if
1070 cohesive forces are weaker than on average, as it is the case in Iceland, the entrainment threshold for
1071 dust-size particles can be reduced to a value similar to or possibly even lower than for sand-size
1072 particles, enabling efficient direct aerodynamic dust emission without saltation as an intermediate
1073 process (Klose and Shao, 2013; Shao and Klose, 2016).

1074 In contrast to Saharan dust-emitting sediments, which comprise quartz, feldspars, clays, calcite,
1075 dolomite, hematite/goethite, and halite, sediments from Iceland's dust sources are predominantly
1076 composed of amorphous [phases and](#) volcanic glass. They also contain anorthite (Ca-plagioclase),
1077 augite (pyroxene), and andesine (plagioclase), with smaller quantities of analcime, magnetite, Ca-
1078 modernite, and hematite. These pronounced differences in composition have distinct implications for
1079 ice nucleation, radiative forcing, and nutrient deposition. While the effects of the main minerals in hot
1080 deserts on these processes are relatively well-understood, the impact of volcanic glass, which
1081 constitutes the majority of Icelandic dust, remains largely unexplored and requires further research.
1082 One notable difference is the average iron (FeT) content in Icelandic sediments, which is
1083 approximately three times higher than that in Saharan sediments. Additionally, the proportion of FeS
1084 in FeT is greater in Iceland than in the Sahara, comprising 79 % vs 67 % for top sediments, 82 % vs 68
1085 % for underlying fluvial sediments, and 80 % vs 73 % for [aeolian ripples](#) (as detailed in Table [2](#) and
1086 Figure [15](#)). The proportion of Fe from hematite and goethite (FeD %) in Iceland is lower than in the
1087 Sahara (1-7 % vs 31 %) while the proportion of FeM is higher in Iceland (9.5-18 % vs negligible) yielding
1088 to a potentially different climate effect from the emitted dust (Table [2](#) and Figure [15](#)). Furthermore,
1089 the proportion of FeA, which is highly bioavailable, is lower in Iceland for top sediments (1.3 % vs. 1.9
1090 % of the FeT content), fluvial sediments (1.2 % vs. 1.4 %), and [aeolian ripples](#) (0.85 % vs. 1.0 %) (as
1091 shown in Table [2](#) and Figure [15](#)). It is important to note that, even though the % FeA in Icelandic
1092 sediments is slightly lower, the amount of bioavailable Fe per mass in Iceland's dust-emitting
1093 sediments is higher than that of Saharan sediments due to the higher FeT contents in Icelandic
1094 samples. Similar mineralogical content was found by Baldo et al. (2020), with a major proportion of
1095 volcanic glass in the sediments, followed by anorthite and augite at Dyngjuvatn and Hagavatn. Fe
1096 proportions and total amount are also very similar to those obtained by Baldo et al. (2020).

1097 Spectra of dust source sediments from Morocco are markedly different than those from Iceland as
1098 seen also in the mineralogy (Figure [8a](#), b, and c). Spectra from Morocco have electronic transitions
1099 and charge transfers of Fe³⁺ at wavelengths <1 μm, related to hematite and goethite presence (Figure
1100 [8a](#), b, and c), whereas spectra from Iceland have broader Fe²⁺ electronic transitions at wavelengths >1
1101 μm and sometimes near 2 μm, related to the volcanic glass and pyroxene proportion (Figure [8c](#)). At
1102 longer wavelengths, spectra of sediments from Morocco show features of phyllosilicates, including
1103 illites and smectites, whereas in Iceland this is not observed, except the 2.2 μm feature in Figure [8](#)
1104 may be due to hydrated silica plus phyllosilicates such as montmorillonite.

1105 **3.7. Conceptual model for dust emission, particle size and mineralogy for Dyngjusandur, a major** 1106 **Iceland dust hotspot**

1107 Dust-emission in Iceland is primarily governed by glaciofluvial environments. These regions are
1108 characterized by the melting of glaciers that have accumulated substantial [fine](#) volcanic ash over
1109 geological time. Subsequently, the fluvial [streams](#), transport significant quantities of fine materials,

Eliminado: 4

Eliminado: 14

Eliminado: 4

Eliminado: 14

Eliminado: 4

Eliminado: 14

Eliminado: 7a

Eliminado: 7a

Eliminado: 7c

Eliminado: micron

Eliminado: 7

Eliminado: 5. A

Eliminado: c

Eliminado: sediments and

Eliminado: erosion

Eliminado: of these sediments

Eliminado: s

1127 which are deposited in extensive, flat areas during floods (Figure 16). The fine nature of the sediments
1128 can be attributed to several factors. Firstly, to the fine volcanic ash preserved in the melting ice.
1129 Secondly, particle size segregation occurs during transportation from the moraine to the flooding
1130 plains. Additionally, the recycling of aeolian dust may play a significant role. Dust emitted from the
1131 plains is redeposited in the ice and surface sediments of the basin, eventually washed out towards the
1132 plains during subsequent events. Furthermore, the accumulation of fine- and light-particle pumice top
1133 layers in the ponded areas of the lowlands, also favour the emission of dust. These processes are
1134 particularly prevalent in the Jokulsá á Fjöllum basin and other similar locations like Dyngjuvatn,
1135 Mælifellsandur, and Mýrdalssandur, with heightened activity during the summer months when glacial
1136 melting accelerates. Once these deposited fine sediments dry out, they become prone to dust
1137 emission when appropriate wind patterns prevail.
1138 In the Jökulsá á Fjöllum basin, this scenario is generated thanks to the natural dam created after the
1139 Bardabunga eruption, when fluvial channels deposit large volumes of sediments across Dyngjusandur,
1140 a flat and extensive region (Figure 16). In this endorheic flat, continuous summer floods lead to cyclic
1141 sediment deposition. Coarser fluvial sediments are deposited first and are subsequently covered by
1142 top sediments of very fine grains formed after each cycle through the deposition of suspended fine
1143 particles following drying or infiltration of ponded waters (Figure 17). The frequency of flooding was
1144 nearly daily under insolation, and this leaves a cyclic pattern (top sediment, fluvial sediments) in the
1145 sedimentary record. Thus, in sunny days of August there was a typical daily cycle of midday to late
1146 afternoon flooding followed by drying and dust emission the next day. Also, during intensive flooding
1147 episodes, a large amount of top sediments covers very large surfaces, and if sunny days or adequate
1148 synoptic flows occur the subsequent day, high dust emissions are recorded. Following sediment
1149 deposition, waters infiltrate and traverse the lava field, flowing to the other side of the natural dam
1150 with minimal sediment load. On the other side of the dam, these pristine waters join those from the
1151 other channels unaffected by the dam and flow toward the sea. Because the dam stops part of the
1152 floods and because the river is more incised, overflows and sediment flats alongside the river are very
1153 reduced from the dam to the sea. However, large flooding flats at the sea once again contain
1154 sediments prone to dust emission. Such sedimentation, particle size fractionation, drying and dust
1155 emission processes are generally repeated daily under favourable conditions in summer. The aeolian
1156 ripples are formed in the dry part of the cycle and can be mobilised by the wind and trigger the
1157 emission of dust by saltation. However, the lack of cohesive forces in the sediments may also allow
1158 direct aerodynamic entrainment of dust at lower wind speeds without the need of saltation (Figure
1159 17).

1160 4. Conclusions

1161 This study has undertaken a comprehensive examination of dust-emitting sediments in Iceland,
1162 focusing on their particle size distributions, mineralogy, and Fe mode of occurrence. Our findings
1163 reveal distinctive characteristics among various sites, with Hagavatn and Dyngjusandur exhibiting the
1164 finest particle size distributions, and Mýrdalssandur and Dyngjuvatn showing the coarsest. Despite
1165 these variations, the overall particle size distributions in Iceland's top sediments, whether fully or
1166 minimally dispersed, exhibit remarkable similarities. Notably, these distributions sharply contrast with
1167 those observed in a dust hotspot in the Moroccan Sahara. Iceland's top sediments are approximately
1168 four times coarser than fully dispersed Moroccan crusts, yet, these fully dispersed Iceland top
1169 sediments are finer than the minimally dispersed Moroccan crusts, prevalent in the Moroccan Sahara.

Eliminado: 15

Eliminado: is phenomenon is

Eliminado: ¶

Eliminado: 16

Eliminado: 16

Eliminado: 6

Eliminado: minerally

1177 These distinctions underscore the relatively limited interparticle cohesion in Iceland, a characteristic
1178 that sets it apart. The scarcity of cohesion implies an efficient saltation bombardment process, and at
1179 the same time suggests the possibility of direct aerodynamic entrainment of dust in this region. This
1180 contrasts with the cohesive sediments typically found in hot desert environments, where interparticle
1181 cohesion hinders dust aerodynamic entrainment, making saltation the primary mechanism for dust
1182 emission.

1183 Iceland's dust-emitting sediments primarily consist of black volcanic glass or amorphous phases,
1184 constituting a substantial proportion ranging from 70% to 85% by weight. Plagioclase and pyroxenes
1185 contribute 10% to 15% and 4% to 8%, respectively, with traces of zeolites and Fe-oxides present.
1186 Consistent compositional patterns emerge across most dust-emitting regions in Iceland, except for
1187 Landeyjarsandur and Hagavatn. In these regions, sediments display diminished glass content (35% and
1188 <0.1%, respectively) and heightened levels of plagioclase and pyroxenes, reaching up to 65% and 31%,
1189 respectively. These compositional variations are starkly distinct from Saharan dust-emitting
1190 sediments, owing to the differing volcanic and sedimentary origins of the respective dust sources.
1191 Notably, in Saharan sediments, the presence of salts, carbonates, and clays promotes the formation
1192 of aggregates that increase particle size and sediment cohesion. The composition of Fe-oxides also
1193 varies between the two regions, with hematite and goethite being predominant in the Sahara, while
1194 Iceland's sediments predominantly contain magnetite. The specific role of black volcanic glass in dust-
1195 radiation and dust-cloud interactions remains inadequately described, contributing to a limited
1196 understanding of its impact on climate. Further research is essential to unravel the complexities of
1197 these interactions and their implications for climate.

1198 The distribution of Fe in the top sediments of Jökulsá á Fjöllum, as well as in the underlying fluvial
1199 sediments and the aeolian ripples, exhibits homogeneity in its mode of occurrence. The averaged bulk
1200 Fe content (FeT) is 9.5 ± 0.40 %wt, with structural Fe (FeS) constituting $80 \pm 6.3\%$, and Fe in magnetite
1201 (FeM) accounting for $16 \pm 5.5\%$. Minor variations are observed in the proportions of Fe as
1202 hematite/goethite (FeD) and readily exchangeable- and nano-Fe (FeA). Notably, the top sediments
1203 display a significant presence of readily exchangeable Fe and hematite/goethite, attributed to
1204 heightened glass weathering in the fine top sediment compared to coarser underlying layers and
1205 aeolian ripples. Similar trends were identified in various Icelandic sources, with Mælifellsandur and
1206 Mýrdalssandur exhibiting higher mean FeT ($11 \pm 0.48\%$ and $11 \pm 0.41\%$, respectively). Hagavatn and
1207 Skaftarsandur showed a maximum proportion of FeA ($2.7 \pm 1.0\%$) and (2.6%, 1 sample), respectively.
1208 Landeyjarsandur displayed the maximum FeD proportion ($7.2 \pm 2.1\%$), while Dyngjusandur exhibited
1209 the highest proportion of FeM ($18 \pm 4.6\%$). In comparison to the Moroccan Saharan, although
1210 proportions are similar, the bulk Fe content in Iceland is threefold higher. Consequently, for the same
1211 emitted dust mass, the absolute mass of FeA is three times greater, with FeD being smaller, and FeM
1212 emerging as the major contributor, resulting in a potentially distinct impact on oceans and terrestrial
1213 ecosystems and yielding diverse implications for climate.

1214 Airborne and in-situ spectroscopy results are broadly consistent with XRD and PSD results. The spectra
1215 of ripples are dark (low albedo) and dominated by primary volcanic phases and show no systematic
1216 trends with distance from the glacier. Top sediments show trends with distance from the glacier
1217 (Figure 13), with the albedo being brighter with increasing distance partly due to decreasing particle
1218 size, which most likely is the result of mechanical sorting, with finer grained hydrated, altered phases

Eliminado: size

Eliminado: 12

1221 becoming more prevalent downstream relative to coarser, unaltered volcanic glass. There is lack of
1222 significant clay minerals, carbonates and salts. The marked differences in composition between
1223 Icelandic and Moroccan sources are also captured. Spectra from Morocco have electronic transitions
1224 and charge transfers of Fe³⁺ at wavelengths <1 μm, related to hematite and goethite, while spectra
1225 from Iceland have broader Fe²⁺ electronic transitions at longer wavelengths, related to the volcanic
1226 glass and pyroxene.

1227 A conceptual model has been formulated to elucidate the elevated dust emissions observed in
1228 Dyngjúsandur, Iceland. This model encompasses several key factors contributing to the phenomenon.
1229 Firstly, the historical entrapment of substantial amounts of fine volcanic ash by the glacier has
1230 established a reservoir of materials awaiting liberation. The accelerated melting of the glacier,
1231 particularly intensified during summer and influenced by underlying volcanism, releases significant
1232 volumes of fresh sediment. Notably, a volcanic field active in 2014-2015 functions as a natural dam,
1233 triggering extensive floods that inundate large plains with sediments prone to inducing dust emissions.
1234 The high pumice top layers in the lowlands also favours dust emissions because the fine and low
1235 density patterns of the pumice particles. The emitted dust can be deposited on the ice of the glacier
1236 and the surfaces of the basin, and in turn be washed out towards the plains of the lowlands during
1237 subsequent flooding episodes and rain. These floods are recurrent under specific summer conditions
1238 (high insolation and temperature) causing melting of ice leading to flooding, and fostering particle
1239 sedimentation and fractionation. Subsequently, dry weather and high wind patterns facilitate dust
1240 emission.

1241 The inherent nature of the sediments, characterized by black basalt detritus and volcanic ash with a
1242 predominant glassy composition, results in minimal particle aggregation and cohesion. Moreover, the
1243 frequent and extensive vertical particle size segregation during the flooding cycles contributes to the
1244 coverage of vast areas with very fine sediments, thereby facilitating dust emission. Numerous studies
1245 (Flowers et al., 2005; Magnusson et al., 2005; Hauser and Schmitt, 2021) have highlighted the region's
1246 high sensitivity to climate change, with projections suggesting increased ice melting in the future.
1247 These conditions are expected to further exacerbate dust emissions, indicating a potential escalation
1248 in the future.

1249
1250 The synergy of these geological, climatic, and environmental factors provides a comprehensive
1251 understanding of the intricate processes driving high dust emissions in Dyngjúsandur.

1252 **Code availability.** The code used in this paper is provided by Clark (2023, <https://github.com/PSI->
1253 [edu/spectroscopy-tetracorder](https://github.com/PSI-edu/spectroscopy-tetracorder)).

1254 **Data availability.** Data used in this paper are given in the main paper itself and in the Supplement. If
1255 **needed, data are also available upon request by emailing the authors.**

1256 **Author contributions.** CPG-P proposed and designed the field campaign with contributions of AA, KK,
1257 MK and XQ. The Campaign was implemented by CPG-P, AA, CGF, AGR, KK, MK, AP, XQ and JYD. The
1258 samples were collected by CPG-P, AA, AGR, MK, AK, RG and XQ and analysed by AGR, PC and NM.
1259 Spectroscopy was analysed by AK, RG, BLE, PB and RNC. AGR performed the visualization and writing
1260 of the original draft manuscript and CPG-P and XQ supervised the work. CPG-P and XQ re-edited the
1261 manuscript and all authors contributed in data discussion, reviewing and manuscript finalization.

Eliminado: sediments and

Eliminado: ¶

Eliminado: exhibit a daily recurrence

Eliminado: ,

Eliminado: particle

Eliminado: (

Eliminado:),

Eliminado: (

Eliminado:)

Eliminado: (

Eliminado:)

Eliminado:

1274 **Competing interests.** At least one of the (co-)authors is a member of the editorial board of
1275 Atmospheric chemistry and Physics.

1276 **Acknowledgements**

1277 The field campaign and its associated research, including this work, was funded by the European
1278 Research Council under the Horizon 2020 research and innovation programme through the ERC
1279 Consolidator Grant FRAGMENT (grant agreement No. 773051) and the AXA Research Fund through
1280 the AXA Chair on Sand and Dust Storms at BSC. CGF was supported by a PhD fellowship from the
1281 Agència de Gestió d'Ajuts Universitaris i de Recerca (AGAUR) grant 2020_FI B 00678. KK was funded
1282 by the Deutsche Forschungsgemeinschaft (DFG, German Research Foundation) – 264907654;
1283 416816480. MK has received funding through the Helmholtz Association's Initiative and Networking
1284 Fund (grant agreement no. VH-NG-1533). We acknowledge the EMIT project, which is supported by
1285 the NASA Earth Venture Instrument program, under the Earth Science Division of the Science Mission
1286 Directorate. We thank Dr. Eva L. Scheller for the help during the field spectroscopy measurements.
1287 We thank Dr. Pavla Dagsson Waldhauserova from the Agricultural university of Iceland for the
1288 invaluable support and help during the field campaign. We thank Thomas Dirsch for the uncountable
1289 driving hours and mechanical support during the soil sampling. We thank Paul Ginoux for providing
1290 high-resolution global dust source maps, which were very helpful for the identification of the
1291 FRAGMENT experimental sites. We thank the staff from the ranger station at Dreki as well as the
1292 wardens of the Dreki campsite and the Dreki mountain rescue service for their valuable support and
1293 advice. We also thank Vilhjalmur Vernharðsson and his crew from Fjalladýrð for their permanent
1294 logistic help. Without all of them, the measurement campaign would not have been successfully
1295 feasible.

1296 **7. References**

- 1297 Anderson J.H. and Wickersheim K.A.: Near Infrared Characterization of Water and Hydroxyl Groups on
1298 Silica Surfaces. *Surface Science* 2, 252–60, 1964. [https://doi.org/10.1016/0039-](https://doi.org/10.1016/0039-6028(64)90064-0)
1299 [6028\(64\)90064-0](https://doi.org/10.1016/0039-6028(64)90064-0).
- 1300 Arnalds Ó., Gísladóttir F.O., Sigurjonsson H.: Sandy deserts of Iceland: an overview. *Journal of Arid*
1301 *Environments*, 47, 3, 359-371, 2001.
- 1302 Arnalds Ó.: Dust sources and deposition of aeolian materials in Iceland. *Icelandic agricultural sciences*,
1303 23, 3-21, 2010.
- 1304 Arnalds Ó., Olafsson H. and Dagsson-Waldhauserova P.: Quantification of iron-rich volcanogenic dust
1305 emissions and deposition over the ocean from Icelandic dust sources, *Biogeosciences*, 11,
1306 6623-6632. <https://doi.org/10.5194/bg-11-6623-2014>, 2014.
- 1307 Arnalds Ó., Dagsson-Waldhauserova P., Olafsson H.: The Icelandic volcanic aeolian environment:
1308 Processes and impacts — A review. *Aeolian Research*, 20, 176-195, 2016.
- 1309 Arnalds Ó., Dagsson-Waldhauserova P., Olafsson H.: Dyngjúsandur: a rapidly evolving hyperactive dust
1310 source north of Vatnajökull glacier, Iceland. *Geophysical Research Abstracts*, 20, EGU2018-
1311 14764, 2018.
- 1312 Baldo C., Formenti P., Nowak S., Chevaillier S., Cazaunau M., Pangui E., Di Baggio C., Doussin J.F.,
1313 Ignatyev K., Dagsson-Waldhauserova P., Arnalds O., MacKenzie A.R., Shi Z.: Distinct chemical
1314 and mineralogical composition of Icelandic dust compared to Northern African and Asian dust.
1315 *Atmospheric Chemistry and Physics*, 20, 13521-13539, 2020.

1316 Baldo C., Formenti P., Di Biagio C., Lu G., Song C., Cazaunau M., Pangui E., Doussin J.-F., Dagsson-
1317 Waldhauserova P., Arnalds O., Beddows D., MacKenzie A.R., Shi Z.: Complex refractive index
1318 and single scattering albedo of Icelandic dust in the shortwave spectrum, *EGUsphere*
1319 [preprint], <https://doi.org/10.5194/egusphere-2023-276>, 2023.

1320 Baratoux D., Mangold N., Arnalds O., Bardintzeff J.M., Platevoët B., Grégoire M. and Pinet P.: Volcanic
1321 sands of Iceland - Diverse origins of aeolian sand deposits revealed at Dyngjusandurand
1322 Lambahraun. *Earth Surf. Process. Landforms*, Vol.36, 1789-1808, 2011.

1323 Beckett F., Kylling A., Sigurðardóttir G., von Löwis S., Witham C.: Quantifying the mass loading of
1324 particles in an ash cloud remobilized from tephra deposits on Iceland, *Atmos. Chem. Phys.*,
1325 17, 4401–4418, <https://doi.org/10.5194/acp-17-4401-2017>, 2017.

1326 Bell P.M., Mao H.K., and Weeks R.A.: Optical Spectra and Electron Paramagnetic Resonance of Lunar
1327 and Synthetic Glasses - A Study of the Effects of Controlled Atmosphere, Composition, and
1328 Temperature. *Proc. Lunar Sci. Conf. 7*, p. 2543–59, 1976.

1329 Bishop J.L., Lane M.D., Dyar M.D., and Brown A.J.: Reflectance and Emission Spectroscopy Study of
1330 Four Groups of Phyllosilicates: Smectites, Kaolinite-Serpentines, Chlorites and Micas." *Clay*
1331 *Minerals* 43, 1, 35–54, 2008. <https://doi.org/10.1180/claymin.2008.043.1.03>.

1332 Brodrick, P.G., Thompson, D.R., Fahlen, J.E., Eastwood, M.L., Sarture, C.M., Lundeen, S.R., Olson-
1333 Duvall, W., Carmon, N., Green, R.O.: Generalized radiative transfer emulation for imaging
1334 spectroscopy reflectance retrievals. *Remote Sens. Environ.* 261, 112476, 2021

1335 Bullard J.E.: Contemporary glacial inputs to the dust cycle. *Earth Surf. Proc. Land.*, 38, 71-89.
1336 <https://doi.org/10.1002/esp.3315>, 2013.

1337 Bullard J.E., Baddock M., Bradwell T., Crusius J., Darlington E., Gaiero D., Gassó S., Gisladottir G.,
1338 Hodgkins R., McCulloch R., McKenna-Neuman C., Mockord T., Stewart H., Thorsteinsson T.:
1339 High-latitude dust in the Earth system. *Reviews of Geophysics*, 54, 447-485.
1340 doi:10.1002/2016RG000518, 2016.

1341 Burns R.G.: *Mineralogical Applications of Crystal Field Theory*. Cambridge University Press, 1993.

1342 Castellanos A.: The Relationship Between Attractive Interparticle Forces and Bulk Behaviour in Dry and
1343 Uncharged Fine Powders. *Advances in Physics*, 54, 4, 263-376, 2005.

1344 [Carrivick, J.L., & Tweed, F.S.: A review of glacier outburst floods in Iceland and Greenland with a](#)
1345 [megafloods perspective. *Earth-Science Reviews*, 196, 102876, 2019.](#)

1346 Cheary R.W., Coelho A.: A fundamental parameters approach to X-ray line profile fitting. *Journal of*
1347 *Applied Crystallography* 25, 109–121, 1992.

1348 Claquin T., Schulz M., Balkanski Y.J.: Modeling the mineralogy of atmospheric dust sources. *Journal*
1349 *Geophysical Research*. 104, D18, 22243-22256, 1999.

1350 Clark R.N., and Roush T.L.: Reflectance Spectroscopy: Quantitative Analysis Techniques for Remote
1351 Sensing Applications. *Journal of Geophysical Research*, 89, B7, 6329-6340, 1984.
1352 <https://doi.org/10.1029/JB089iB07p06329>.

1353 Clark R.N., King T.V.V., Klejwa M., Swayze G.A., and Vergo N.: High Spectral Resolution Reflectance
1354 Spectroscopy of Minerals. *Journal of Geophysical Research* 95, no. B8, 12653–80, 1990.
1355 <https://doi.org/199010.1029/JB095iB08p12653>.

1356 Clark R.N., Swayze G.A., Livo K.E., Kokaly R.F., Sutley S.J., Dalton J.B., McDougal R.R., Gent C.A.: Imaging
1357 spectroscopy: Earth and planetary remote sensing with the USGS Tetracorder and expert
1358 systems. *The Journal of Geophysical Research*, v.108, 2003. doi:10.1029/2002JE001847.

1359 Clark, R. N., Swayze, G. A., Livo, K. E., Brodrick, P., Noe Dobrea, E., Vijayarangan, S., Green, R. O.,
1360 Wettergreen, D., Garza, A. C., Hendrix, A., García-Pando, C. P., Pearson, N., Lane, M., González-

1361 Romero, A., Querol, X. & the EMIT and TREX teams. Imaging spectroscopy: Earth and planetary
1362 remote sensing with the PSI Tetracorder and expert systems: from Rovers to EMIT and
1363 Beyond, *Planetary Science J.*, in review, 2023.

1364 Cloutis E.A., and Gaffey M.J.: Pyroxene Spectroscopy Revisited: Spectral-Compositional Correlations
1365 and Relationship to Geothermometry. *Journal of Geophysical Research* 96, E5, 22,809-22,826,
1366 1991. <https://doi.org/199110.1029/91JE02512>.

1367 Cvetkovic B., Dagsson-Waldhauserova P., Petkovic S., Arnalds O., Madonna F., Proestakis E., Gkikas A.,
1368 Vimic A.V., Pejanovic G., Rosoldi M., Ceburnis D., Amiridis V., Lisá L., Nickovic S., Nikolic J.: Fully
1369 dynamic high-resolution model for dispersion of icelandic airborne mineral dust. *Atmosphere*,
1370 13, 9, 1345. <https://doi.org/10.3390/atmos13091345>, 2022.

1371 [Dagsson-Waldhauserova, P., Arnalds, O., & Olafsson, H.: Long-term variability of dust events in Iceland
1372 \(1949–2011\). *Atmospheric Chemistry and Physics*, 14\(24\), 13411-13422, 2014.](#)

1373 Dagsson-Waldhauserova P., Arnalds O., Olafsson H., Hladil J., Skala R., Navratil T., Chadimova L., and
1374 Meinander O.: Snow–Dust Storm: Unique case study from Iceland, March 6–7, 2013. *Aeolian
1375 Research*, 16, 69-74. <https://doi.org/10.1016/j.aeolia.2014.11.001>, 2015.

1376 Dagsson-Waldhauserova P., Magnúsdóttir A.O., Olafsson H., Arnalds O.: The Spatial Variation of Dust
1377 Particulate Matter Concentrations during Two Icelandic Dust Storms in 2015, 2016.

1378 De la Torre A.G., Bruque S., Aranda M.A.G.: Rietveld quantitative amorphous content analysis. *Journal
1379 of Applied Crystallography*, 34:196-202, 2001.

1380 De Longueville F., Hountondji Y. C., Henry S., Ozer P.: What do we know about effects of desert dust
1381 on air quality and human health in West Africa compared to other regions?. *Sci. Total Environ.*,
1382 409, 1-8, 2010.

1383 Di Biagio C., Formenti P., Balkanski Y., Caponi L., Cazaunau M., Pangui E., Journet E., Nowak S., Andreae
1384 M.O., Kandler K., Saeed T., Piketh S., Seibert D., Williams E., Doussin J.F.: Complex refractive
1385 indices and single-scattering albedo of global dust aerosols in the shortwave spectrum and
1386 relationship to size and iron content. *Atmos. Chem. Phys.*, 19, 15503-15531.
1387 <https://doi.org/10.5194/acp-19-15503-2019>, 2019.

1388 Dragosics M., Meinander O., Jónsdóttir T., Dürig T., De Leeuw G., Pálsson F., Dagsson-Waldhauserova
1389 P., Thorsteinsson T.: Insulation effects of Icelandic dust and volcanic ash on snow and ice.
1390 *Arab. J. Geosci.*, 9, 126, <https://doi.org/10.1007/s12517-015-2224-6>, 2016.

1391 Engelbrecht J.P., Moosmüller H., Pincock S., Jayanty R.K.M., Lersch T., Casuccio G.: Technical note:
1392 Mineralogical, chemical, morphological, and optical interrelationships of mineral dust re-
1393 suspensions. *Atmos. Chem. Phys.*, 16, 10809-10830. [https://doi.org/10.5194/acp-16-10809-
1394 2016](https://doi.org/10.5194/acp-16-10809-2016), 2016.

1395 Einarsson M.A.: Climate of Iceland. Van. Loon (Ed.), *World Survey of Climatology*, 15, Chapter 7,
1396 Elsevier, Amsterdam, 672-697. *Atmosphere*, 7(6), 77.
1397 <https://doi.org/10.3390/atmos7060077>, 1984.

1398 [Flowers, G.E., Marshall, S.J., Björnsson, H., & Clarke, G.K.: Sensitivity of Vatnajökull ice cap hydrology
1399 and dynamics to climate warming over the next 2 centuries. *Journal of Geophysical Research:
1400 Earth Surface*, 110\(F2\), 2005.](#)

1401 Formenti P., Caqueneau S., Chevaillier S., Klaver A., Desboeufs K., Rajot J.L., Belin S., Briois V.:
1402 Dominance of goethite over hematite in iron oxides of mineral dust from Western Africa:
1403 Quantitative partitioning by X-ray absorption spectroscopy. *J. Geophys. Res. Atmos.*, 119,
1404 12740-12754. <https://doi.org/10.1002/2014jd021668>, 2014.

1405 Geiger H., Mattson T., Deegan F.M., Troll V.R., Burchardt S., Gudmundsson Ó., Tryggvason A.,
1406 Krumbholz M., Harris C.: Magma plumbing for the 2014–2015 Holuhraun eruption, Iceland.
1407 *Geochemistry, Geophysics, Geosystems*, 17, 8, 2953–2968, 2016.

1408 [Gonçalves Ageitos, M., Obiso, V., Miller, R. L., Jorba, O., Klose, M., Dawson, M., Balkanski, Y., Perlwitz,](#)
1409 [J., Basart, S., Di Tomaso, E., Escribano, J., Macchia, F., Montané, G., Mahowald, N. M., Green,](#)
1410 [R. O., Thompson, D. R., and Pérez García-Pando, C.: Modeling dust mineralogical composition:](#)
1411 [sensitivity to soil mineralogy atlases and their expected climate impacts, *Atmos. Chem. Phys.*,](#)
1412 [23, 8623–8657, <https://doi.org/10.5194/acp-23-8623-2023>, 2023.](#)

1413 González-Flórez C., Klose M., Alastuey A., Dupont S., Escribano J., Etyemezian V., Gonzalez-Romero A.,
1414 Huang Y., Kandler K., Nikolich G., Panta A., Querol X., Reche C., Yus-Díez J., Pérez García-Pando
1415 C.: Insights into the size-resolved dust emission from field measurements in the Moroccan
1416 Sahara, *Atmos. Chem. Phys.*, 23, 7177–7212, <https://doi.org/10.5194/acp-23-7177-2023>,
1417 2023.

1418 [González-Flórez, C., Klose, M., Alastuey, A., Dagsson-Waldhauserová, P., Dupont, S., Escribano, J.,](#)
1419 [González-Romero, A., Irvine, M., Kandler, K., Panta, A., Querol, X., Schepanski, K., Yus-Díez, J.,](#)
1420 [and Pérez García-Pando, C.: Comparing the emitted dust particle size distribution in Iceland](#)
1421 [and Morocco from intensive field measurements. Abstract \(AE14B-1234\) presented at AGU23,](#)
1422 [11-15 Dec, 2023.](#)

1423 González-Romero A., González-Florez C., Panta A., Yus-Díez J., Reche C., Córdoba P., Moreno N.,
1424 Alastuey A., Kandler K., Klose M., Baldo C., Clark R.N., Shi Z.B., Querol X., Pérez García-Pando
1425 C.: Variability in grain size, mineralogy, and mode of occurrence of Fe in surface sediments of
1426 preferential dust-source inland drainage basins: The case of the Lower Drâa Valley, S Morocco.
1427 *EGUsphere* [preprint], <https://doi.org/10.5194/egusphere-2023-1120>, 2023.

1428 [González-Romero, A., González-Flórez, C., Panta, A., Yus-Díez, J., Córdoba, P., Alastuey, A., Moreno,](#)
1429 [N., Hernández-Chiriboga, M., Kandler, K., Klose, M., Clark, R. N., Ehlmann, B. L., Greenberger,](#)
1430 [R. N., Keebler, A. M., Brodrick, P., Green, R., Ginoux, P., Querol, X., and Pérez García-Pando,](#)
1431 [C.: Characterization of the particle size distribution, mineralogy and Fe mode of occurrence of](#)
1432 [dust-emitting sediments across the Mojave Desert, California, USA, *EGUsphere* \[preprint\],](#)
1433 <https://doi.org/10.5194/egusphere-2024-434>, 2024.

1434 Goryniuk M.C., Rivard B.A., and Jones B.: The Reflectance Spectra of Opal-A (0.5–25 Mm) from the
1435 Taupo Volcanic Zone: Spectra That May Identify Hydrothermal Systems on Planetary Surfaces.
1436 *Geophysical Research Letters* 31, 24, 2004. <https://doi.org/10.1029/2004GL021481>.

1437 Goudie A.S. & Middleton N.J.: Desert dust in the global system. Springer, Heidelberg. ISBN 978-786 3-
1438 540-32355-6, 288 pp, 2006.

1439 Green R.O., Mahowald N., Ung C., Thompson D.R., Bator L., Bennet M., Zan J.: The earth surface
1440 mineral dust source investigation: an earth science imaging spectroscopy mission. In: IEEE
1441 Aerospace Conference Proceedings. IEEE Computer Society.
1442 <https://doi.org/10.1109/AERO47225.2020.9172731>. 2020.

1443 Groot Zwaaftink C.D., Arnalds Ó., Dagsson-Waldhauserova P., Eckhardt S., Prospero J.M., Stohl A.:
1444 Temporal and spatial variability of Icelandic dust emissions and atmospheric transport, *Atmos.*
1445 *Chem. Phys.*, 17, 10865–10878, <https://doi.org/10.5194/acp-17-10865-2017>, 2017.

1446 [Hauser, S., & Schmitt, A.: Glacier retreat in Iceland mapped from SPACE: Time series analysis of](#)
1447 [geodata from 1941 to 2018. *PFG–Journal of Photogrammetry, Remote Sensing and*](#)
1448 [Geoinformation Science](#), 89(3), 273–291, 2021.

1449 Horgan, B.H.N., Cloutis E.A., Mann P., and Bell J.F.: Near-Infrared Spectra of Ferrous Mineral Mixtures
1450 and Methods for Their Identification in Planetary Surface Spectra. *Icarus* 234, 132–54, 2014.
1451 <https://doi.org/10.1016/j.icarus.2014.02.031>.

1452 Ibáñez J., Font O., Moreno N., Elvira J.J., Alvarez S., Querol X.: Quantitative Rietveld analysis of the
1453 crystalline and amorphous phases in coal fly ashes. *Fuel*, 105: 314–317, 2013.

1454 Jickells T.D., An Z.S., Andersen K.K., Baker A.R., Bergametti G., Brooks N., Cao J.J., Boyd P.W., Duce
1455 R.A., Hunter K.A., Kawahata H., Kubilay N., Laroche J., Liss P.S., Mahowald N., Prospero J.M.,
1456 Ridgwell A.J., Tegen I., Torres R.: Global iron connections between desert dust, ocean
1457 biogeochemistry, and climate. *Science*, 308, 5718, 67–71. DOI: 10.1126/science.1105959,
1458 2005.

1459 Johnson M.S., Meskhidze N., Solmon F., Gassó S., Chuang P.Y., Gaiero D.M., Yantosca R.M., Wu S.,
1460 Wang Y., Carouge C.: Modeling dust and soluble iron deposition to the South Atlantic Ocean.
1461 *J. Geophys. Res.*, 115, D15202, doi:10.1029/2009JD013311, 2010.

1462 Journet E., Balkanski Y., Harrison S.P.: A new data set of soil mineralogy for dust-cycle modeling.
1463 *Atmos. Chem. Phys.*, 14, 8, 3801–3816, 2014.

1464 Karanasiou A., Moreno N., Moreno T., Viana M., de Leeuw F., Querol X.: Health effects from Sahara
1465 dust episodes in Europe: Literature review and research gaps. *Environ. Int.* 47, 107–14, 2012.

1466 Klose M. and Shao Y.: Large-eddy simulation of turbulent dust emission, *Aeolian Res.*, 8, 49–58,
1467 <https://doi.org/10.1016/j.aeolia.2012.10.010>, 2013.

1468 Kokaly R.F., Clark R.N., Swayze G.A., Livo K.E., Hoefen T.M., Pearson N.C., Wise R.A., Benzel W.M.,
1469 Lowers H.A., Driscoll R.L.: USGS Spectral Library Version 7. U.S. Geological Survey Data Series
1470 1035, 61 p, 2017. <https://doi.org/10.3133/ds1035>.

1471 Kok J.F., Adebisi A.A., Albani S., Balkanski Y., Checa-Garcia R., Chin M., Colarco P.R., Hamilton D.S.,
1472 Huang Y., Ito A., Klose M., Li L., Mahowald N.M., Miller R.L., Obiso V., Pérez García-Pando C.,
1473 Rocha-Lima A., Wan J.S.: Contribution of the world's main dust source regions to the global
1474 cycle of desert dust, *Atmos. Chem. Phys.*, 21, 8169–8193, [https://doi.org/10.5194/acp-21-](https://doi.org/10.5194/acp-21-8169-2021)
1475 8169-2021, 2021.

1476 Kok, J.F., Storelvmo T., Karydis V.A., Adebisi A.A., Mahowald N.M., Eva A.T., He C., Leung D.M.: Mineral
1477 dust aerosol impacts on global climate and climate change. *Nat. Rev. Earth Environ.* 4, 71–86,
1478 2023. <https://doi.org/10.1038/s43017-022-00379-5>

1479 Kylling A., Zwaafink C.D.G., Stohl A.: Mineral Dust Instantaneous Radiative Forcing in the Arctic,
1480 *Geophys. Res. Lett.*, 45, 4290–4298, 2018.

1481 Laurent B.; Marticorena B.; Bergametti G.; Léon J.F., Mahowald N.M.: Modeling Mineral Dust
1482 Emissions from the Sahara Desert Using New Surface Properties and Soil Database *J. Geophys.*
1483 *Res.*, 113, D14218, 2008.

1484 Machiels L., Mertens G., Elsen J.: Rietveld Refinement strategy for Quantitative Phase analysis of
1485 Partially Amorphous zeolitized tuffaceous. *GEOLOGICA BELGICA* 13,3, 183-196, 2010.

1486 Madsen I.C., Scarlett N.V.Y., Cranswick L.M.D., Lwin T.: Outcomes of the international union of
1487 crystallography commission on powder diffraction round robin on quantitative phase analysis:
1488 Samples 1a to 1h. *J. Appl. Crystallogr.*, 34, pp. 409–426, 2001.

1489 [Magnússon, E., Björnsson, H., Dall, J., & Pálsson, F.: The 20th century retreat of ice caps in Iceland](#)
1490 [derived from airborne SAR: W-Vatnajökull and N-Mýrdalsjökull. *Earth and Planetary Science*](#)
1491 [Letters, 237\(3-4\), 508-515, 2005.](#)

1492 Mahowald N.M., Baker A.R., Bergametti G., Brooks N., Duce R.A., Jickells T.D., Kubilay N., Prospero
1493 J.M., Tegen I.: Atmospheric global dust cycle and iron inputs to the ocean, *Global Biogeochem.*
1494 *Cy.*, 19(4), GB4025, doi:10.1029/2004GB002402, 2005.

1495 Matsui H., Yamane M., Tonami T., Nagami T., Watanabe K., Kishi R., Kitagawa Y., Nakano M.:
1496 Theoretical study on gigantic effect of external static electric field application on nonlinear
1497 optical properties of 1,2,3,5-dithiadiazolyl π -radical dimer. *Mater. Chem. Front.*, 2, 785–790,
1498 DOI: 10.1039/C7QM00549K, 2018.

1499 Meinander O., Dagsson-Waldhauserova P., Amosov P., Aseyeva E., Atkins C., Baklanov A., Baldo C.,
1500 Barr S.L., Barzycka B., Benning L.G., Cvetkovic B., Enchilik P., Frolov D., Gassó S., Kandler K.,
1501 Kasimov N., Kavan J., King J., Koroleva T., Krupskaya V., Kulmala M., Kusiak M., Lappalainen H.
1502 K., Laska M., Lasne J., Lewandowski M., Luks B., McQuaid J.B., Moroni B., Murray B., Möhler
1503 O., Nawrot A., Nickovic S., O’Neill N.T., Pejanovic G., Popovicheva O., Ranjbar K., Romanias M.,
1504 Samonova O., Sanchez-Marroquin A., Schepanski K., Semenkov I., Sharapova A., Shevnina E.,
1505 Shi Z., Sofiev M., Thevenet F., Thorsteinsson T., Timofeev M., Umo N.S., Uppstu A., Urupina
1506 D., Varga G., Werner T., Arnalds O., Vukovic Vimic A.: Newly identified climatically and
1507 environmentally significant high-latitude dust sources. *Atmos. Chem. Phys.*, 22, 11889–11930,
1508 <https://doi.org/10.5194/acp-22-11889-2022>, 2022.

1509 Möller R., Möller M., Kukla P.A., Schneider C., Römer W., Lehmkühl F., Gudmundsson M.T.: Analyzing
1510 relationships between geochemical composition, spectral reflectance, broad-band albedo and
1511 thickness of supra-glacial tephra deposits from the eruptions of Eyjafjallajökull and Grímsvötn
1512 volcanoes in 2010 and 2011. *Am. Geoph. Union, Fall meeting, abstract #C13B-082*, 2016.

1513 Möller R., Möller M., Kukla P.A., Schneider C.: Modulation of glacier ablation by tephra coverage from
1514 Eyjafjallajökull and Grímsvötn volcanoes, Iceland: an automated field experiment. *Earth Syst.*
1515 *Sci. Data*, 10, 53-60, <https://doi.org/10.5194/essd-10-53-2018>, 2018.

1516 Murray B.J., Carslaw K.S. and Field P.R.: Opinion: Cloud-phase climate feedback and the importance
1517 of ice-nucleating particles. *Atmospheric Chemistry and Physics*, 21, 2, 665-679.
1518 <https://doi.org/10.5194/acp-21-665-2021>, 2021.

1519 Oerlemans J., Giesen R., Van Den Broeke M.: Retreating alpine glaciers: Increased melt rates due to
1520 accumulation of dust (Vadret da Morteratsch, Switzerland). *Journal of Glaciology*, 55(192),
1521 729-736. doi:10.3189/002214309789470969, 2009.

1522 Ólafsson H., Furger M., Brümmer B.: The weather and climate of Iceland. *Meteorologische Zeitschrift*,
1523 16, 1, 005-008. <https://doi.org/10.1127/0941-2948/2007/0185>, 2007.

1524 Palacios D., Hughes D.H., García-Ruiz J.M. (eds.): *European Glacial Landscapes. The last deglaciation.*
1525 Elsevier. Amsterdam. ISBN 9780323918992, 2021.

1526 Panta A., Kandler K., Alastuey A., González-Flórez C., González-Romero A., Klose M., Querol X., Reche
1527 C., Yus-Díez J., Pérez García-Pando, C.: Insights into the single-particle composition, size,
1528 mixing state, and aspect ratio of freshly emitted mineral dust from field measurements in the
1529 Moroccan Sahara using electron microscopy, *Atmos. Chem. Phys.*, 23, 3861–3885,
1530 <https://doi.org/10.5194/acp-23-3861-2023>, 2023.

1531 Pérez García-Pando C., Stanton M.C., Diggle P.J., Trzaska S., Miller R.L., Perlwitz J.P., Baldasano J.M.,
1532 Cuevas E., Ceccato P., Yaka P., Thomson M.C.: Soil dust aerosols and wind as predictors of
1533 seasonal meningitis incidence in Niger. *Environ. Health Perspect.* 122, 7679-686, 2014.

1534 Perlwitz J.P., Pérez García-Pando C., and Miller R.L.: Predicting the mineral composition of dust
1535 aerosols – Part 1: Representing key processes. *Atmos. Chem. Phys.*, 15, 11593–11627,
1536 <https://doi.org/10.5194/acp-15-11593-2015>, 2015^a.

1537 Querol X.: The Occurrence and Distribution of Trace Elements in the Teruel Mining District Coals and
 1538 their Behaviour during Coal Combustion. European Coal and Steel Community Project
 1539 7220/ED/014, 1993.

1540 Querol X., Whateley M.K.G., Fernandez-Turiel J.L., Tuncali E.: Geological controls on the mineralogy
 1541 and geochemistry of the Bey pazari lignite, Central Anatolia, Turkey. *Int. J. Coal. Geol.*, 33:255–
 1542 271, 1997.

1543 Rampe E.B., Kraft M.D., Sharp T.G., Golden D.C., Ming D.W., and Christensen P.R.: Allophane Detection
 1544 on Mars with Thermal Emission Spectrometer Data and Implications for Regional-Scale
 1545 Chemical Weathering Processes. *Geology* 40, 11, 995–98, 2012.
 1546 <https://doi.org/10.1130/G33215.1>.

1547 Raupach M.R., Gillette D.A., Leys J.F.: The effect of roughness elements on wind erosion threshold. *J.*
 1548 *Geophys. Res.*, 98, 3023-3029, 1993.

1549 Rietveld H.M.: A profile refinement method for nuclear and magnetic structures. *Journal of Applied*
 1550 *Crystallography* 2, 65–71, 1969.

1551 Sanchez-Marroquin A., Arnalds O., Baustian-Dorsi K.J., Browse J., Dagsson-Waldhauserova P., Harrison
 1552 A.D., Maters E.C., Pringle K.J., Vergara-Temprado J., Burke I.T., Mcquaid J.B., Carslaw K.S.,
 1553 Murray B.J.: Iceland is an episodic source of atmospheric ice-nucleating particles relevant for
 1554 mixed-phased clouds. *Science advances*, 6, 26. DOI: 10.1126/sciadv.aba813, 2020.

1555 Scarlett N. & Madsen I.: Quantification of phases with partial or no known crystal structures. *Powder*
 1556 *Diffraction*, 21(4), 278-284, 2006.

1557 Shao Y. and Lu H.: A simple expression for wind erosion threshold friction velocity, *J. Geophys. Res.-*
 1558 *Atmos.*, 105, 22437–22443, <https://doi.org/10.1029/2000JD900304>, 2000.

1559 Shao Y. and Klose M.: A note on the stochastic nature of particle cohesive force and implications to
 1560 threshold friction velocity for aerodynamic dust entrainment. *Aeolian Res.* 22, 123–125.
 1561 <https://doi.org/10.1016/j.aeolia.2016.08.004>. 2016.

1562 Shi Z.B., Krom M.D., Bonneville S.: Formation of Iron Nanoparticles and Increase in Iron Reactivity in
 1563 Mineral Dust during Simulated Cloud Processing. *Environ. Sci. Technol.* 43, 6592-6596, 2009.

1564 Shi Y., Liu X., Wu M., Zhao X., Ke Z. and Hunter B.: Relative importance of high-latitude local and long-
 1565 range-transported dust for Arctic ice-nucleating particles and impacts on Arctic mixed-
 1566 phased clouds. *Atmospheric Chemistry and Physics*, 22, 4, 2909-2935.
 1567 <https://doi.org/10.5194/acp-22-2909-2022>, 2022.

1568 Sperazza M., Moore J.N., Hendrix M.: High-Resolution particle size analysis of naturally occurring very
 1569 fine-grained sediment through laser diffractometry. *J. Sediment. Res.*, 74(5):736-743, 2004.

1570 Toby, B. H.: R factors in Rietveld analysis: How good is good enough?. *Powder Diffr.*, 21, 67–70,
 1571 <https://doi.org/10.1154/1.2179804>, 2006.

1572 Thompson D.R., Babu K., Braverman A.J., Eastwood M.L., Green R.O., Hobbs J.M., Jewell J.B., Kindel
 1573 B., Massie S., Mishra M.: Optimal estimation of spectral surface reflectance in challenging
 1574 atmospheres. *Remote Sens. Environ.*, 232, 111258,
 1575 <https://doi.org/10.1016/j.rse.2019.111258>, 2019.

1576 Thorsteinsson T., Gísladóttir G., Bullard J., McTainsh G.: Dust storm contributions to airborne
 1577 particulate matter in Reykjavík, Iceland. *Atmospheric Environment*, 45, 32, 5924-5933.
 1578 <https://doi.org/10.1016/j.atmosenv.2011.05.023>, 2011.

1579 Thorpe M.T., Hurowitz J.A., Dehouck E.: Sediment geochemistry and mineralogy from a glacial terrain
 1580 river system in southwest Iceland. *Geochimica et Cosmochimica Acta.* 263, 140-166.
 1581 <https://doi.org/10.1016/j.gca.2019.08.003>, 2019.

1582 TOPAS: TOPAS and TOPAS-Academic: an optimization program integrating computer algebra and
 1583 crystallographic objects written in C++. J. Appl. Cryst. (2018). 51, 210-218, 2018.

1584 Wada K., Arnalds O., Kakuto Y., Wilding L.P., Hallmark C.T.: Clay minerals of four soils formed in eolian
 1585 and tephra materials in Iceland. Geoderma, 52, 3-4, 351-365. [https://doi.org/10.1016/0016-](https://doi.org/10.1016/0016-7061(92)90046-A)
 1586 7061(92)90046-A, 1992.

1587 Wittmann M., Zwaafink C.D.G., Schmidt L.S., Guðmundsson S., Pálsson F., Arnalds O., Björnsson H.,
 1588 Thorsteinsson T., Stohl A.: Impact of dust deposition on the albedo of Vatnajökull ice cap,
 1589 Iceland. The Cryosphere, 11, 741-754, <https://doi.org/10.5194/tc-11-741-2017>, 2017.

1590 Young R.A.: The Rietveld method. International Union of Crystallography. Oxford University Press, UK,
 1591 1993.

1592 Yus-Díez J., Pandolfi M., Alastuey A., González-Florez C., Escribano J., González-Romero A., Ivančič M.,
 1593 Rigler M., Klose M., Kandler K., Panta A., Querol X., Reche C., Pérez García-Pando C.:
 1594 Quantifying variations in multi-wavelength optical properties of freshly-emitted Saharan dust
 1595 from the Lower Drâa Valley, Moroccan Sahara, in preparation, 2023.

1596 Zubko N., Munoz O., Zubko E., Gritsevich M., Escobar-Cerezo J., Berg M. J. and Peltoniemi J.: Light
 1597 scattering from volcanic-sand particles in deposited and aerosol form. Atmospheric
 1598 Environment, 215, 116813. <https://doi.org/10.1016/j.atmosenv.2019.06.051>, 2019.

1599
 1600
 1601

1602 **Figure captions:**

1603 **Figure 1.** Location of Iceland dust hotspots and samples. The green polygon marks the limits of Holuhraun lava
 1604 field. Dashed black lines mark the area of the different dust hotspots in Iceland and dots represent
 1605 samples as top sediments (red), sediments (blue) and aeolian ripples (yellow). Basemap: Imagery data
 1606 from @ Google Earth Pro v: 7.3.6.9345. Jökulsá á Fjöllum is marked as (a) and AVIRIS data flight images
 1607 were used in the zoom in of Dyngjusandur (b) and Dyngjuvatn (c) for a more updated vision of the lakes.
 1608 The yellow star represents the experimental site.

1609 **Figure 2.** Examples of samples collected in Iceland from top sediments (a), fluvial sediments (a) and aeolian
 1610 ripples (b)).

1611 **Figure 3.** 15-min average time series of temperature, winds, volumetric soil water content and dust
 1612 concentration in Dyngjusandur from 12th August to 4th September 2021 (see location in Figure 1). a)
 1613 Ambient temperature at 0.5 m a.g.l. (°C); b) Wind speed measured at 0.4, 0.8, 2.0, 5.0 and 9.9 m above
 1614 ground level (m/s); c) Volumetric water content at depths 2 cm (VWC2), 5 cm (VWC1) and 30 cm (VWC3)
 1615 beneath the surface (%), alongside periods marked by flooding on site (dark blue vertical lines), flooding
 1616 in distance (light blue vertical lines) and rain on site (green vertical lines); d) Total ambient dust
 1617 concentration displayed with a black line (left y-axis) and concentrations for individual size bins
 1618 represented as colour contours, with the corresponding color bar reflecting the concentration ranges.

1619 **Figure 4.** Minimally dispersed particle size distribution (MDPSD) and fully dispersed particle size distribution
 1620 (FDPSD) of top sediment, fluvial sediments and aeolian ripple samples.

1621 **Figure 5.** Mean median diameters of top sediments along the Jökulsá á Fjöllum river, according to the distance
 1622 to the glacier moraine. The grey column indicates the location of the Holuhraun lava field and the red
 1623 vertical line, a tributary channel of Jökulsá á Fjöllum.

1624 **Figure 6.** Particle size distributions of top sediment samples from different dust-emitting hotspots in Iceland as
 1625 determined by MDPSD and FDPSD.

1626 **Figure 7.** Contents of volcanic glass and crystalline minerals in top sediments ($n^{\circ} = 15$), underlying fluvial
 1627 sediments ($n^{\circ} = 8$) and aeolian ripples ($n^{\circ} = 8$) from the Jökulsá á Fjöllum basin.

- Eliminado: Black
- Eliminado: G
- Eliminado: marked
- Eliminado: , and in
- Eliminado: red
- Eliminado: d
- Eliminado: are
- Eliminado: ed
- Eliminado: s
- Eliminado: where
- Eliminado: from
- Eliminado: actualized
- Eliminado: Y
- Eliminado: 3
- Eliminado: 4
- Eliminado: 5
- Eliminado: 6
- Eliminado: e

1646 **Figure 8**, Reflectance spectra measured of surfaces in the field: (a) ripples in Iceland, (b) top sediments in Iceland,
1647 and (c) example spectra from Morocco. In (a) and (b), spectra are offset for clarity and are ordered by
1648 distance from the glacier.

1649 **Figure 9**, Imaging spectrometer data from AVIRIS and analysed with Tetracorder (Clark et al., 2003, 2023). **a)**
1650 Grey scale image of 3 AVIRIS flight lines mosaicked for this study. The white circle if the primary study
1651 area and the grey rectangle is secondary sampling. **b)** Pyroxene composition map. The pyroxene
1652 dominant in the region are clinopyroxenes. **c)** Olivine composition map, which indicates the olivine are
1653 high iron content. However, in areas of significant Fe²⁺ bearing volcanic glass could bias this result. **d)**
1654 Fe²⁺ bearing minerals, which in those area is probably mostly due to volcanic glass. Note few locations
1655 mapped any Fe³⁺ bearing minerals. **e)** Map of 8 minerals with absorptions in the 2-2.5 micron spectral
1656 region. Only trace calcite and outcrops of chlorite/serpentine were found. **f)** Tetracorder map of water
1657 and significant water bearing sediments. Where strong water absorptions are seen, detection of other
1658 minerals is difficult and usually blank in panels **b-f**.

1659 **Figure 10**, Contents of volcanic glass and crystalline minerals in top sediments, underlying fluvial sediments and
1660 aeolian ripples from different dust-emitting hotspots. Dyn: Dyngjusandur, Dvt: Dyngjuvatn, Lan:
1661 Landeyjarsandur, Mýr: Mýrdalsandur, Ska: Skaftarsandur, Mæl: Mælifellsandur, Hgv: Hagavatn.

1662 **Figure 11**, Average percentage of FeS, FeM, FeD and FeA with respect to total Fe content for the Jökulsá á Fjöllum
1663 basin in bars (Y-axis) for top sediments, sediments and ripples. The respective amounts are also
1664 indicated in terms of mg/g, where the denominator refers to g of sediment.

1665 **Figure 12**, Average percentage of FeS, FeM, FeD and FeA for Dyn: Dyngjusandur, Dvt: Dyngjuvatn, Lan:
1666 Landeyjarsandur, Mýr: Mýrdalsandur, Mæl: Mælifellsandur, Hvt: Hagavatn and Ska: Skaftarsandur,
1667 and average amount of each Fe mode of occurrence according to the total content of Fe of the same
1668 dust emitting sources.

1669 **Figure 13**, Trends in infrared spectral features with distance from the glacier. (a) The depth of a broad absorption
1670 feature at 1.035 µm (BD1035) due to Fe²⁺ in volcanic glass and/or pyroxene. (b) The depth of an
1671 absorption feature at 1.9 µm (BD1900) due to H₂O. (c) The depth of an absorption feature at 2.21 µm
1672 (BD2210) due to Si-OH or Al-OH. (d) The albedo (brightness), calculated as the mean reflectance at 1.62-
1673 1.63 µm. Black points are spectra of ripples, and grey are spectra of top sediments.

1674 **Figure 14**, SEM microphotographs of collected dust samples: a) Particles of a top sediment sample from
1675 Dyngjusandur showing dispersed particles. b) Particles of a top sediment sample from the lowlands of
1676 M'Hamid, Morocco (see González-Romero et al., 2023), showing finer particle size and a high degree of
1677 agglomeration. c) Particles from underlying fluvial sediments, from Dyngjusandur, showing a large
1678 particle size and fresh volcanic glassy material. d, e, and f) Samples of top sediments (d and e) from
1679 Dyngjuvatn, showing abundant elongated particles and agglomerates of particles derived from the
1680 breaking of larger pumice particles. g) Image showing particles with magnetite inclusions.

1681 **Figure 15**, Average amount of each Fe mode of occurrence for top sediment JaF: Jökulsá á Fjöllum top sediment
1682 average, Sediment JaF: Jökulsá á Fjöllum sediment average, Ripple JaF: Jökulsá á Fjöllum ripples
1683 average, Dyn: Dyngjusandur, Dvt: Dyngjuvatn, Lan: Landeyjarsandur, Mýr: Mýrdalsandur, Mæl:
1684 Mælifellsandur, Hvt: Hagavatn, Ska: Skaftarsandur, Crust S: Average crust from Sahara, Sediment S:
1685 Average sediment from Sahara and Ripple S: Average ripple from Sahara and average percentage of
1686 FeS, FeM, FeD and FeA normalised by the amount of FeT.

1687 **Figure 16**, Conceptualization of the origin, transport, sedimentation and emission of dust emitting sources,
1688 sediments and dust along Iceland, using the example of the Jökulsá á Fjöllum basin. t1: The glacier feeds
1689 the fluvial systems with fine particles that are transported and size segregated along the basin, t2: in
1690 flat areas or if a volcanic eruption forms a dam, the sediments deposits, t3: under favourable conditions
1691 the dust emission occurs in different parts of the basin by saltation and potentially aerodynamic
1692 entrainment.

1693 **Figure 17**, Example of how particles, mainly volcanic glass with minor proportions of pyroxenes, feldspars and
1694 some iron oxides are transported, segregated and after drying and under favourable conditions, subject
1695 to emission.

Eliminado: 8

Eliminado: 7

Eliminado: 8

Eliminado: A

Eliminado: B

Eliminado: C

Eliminado: D

Eliminado: E

Eliminado: the EMIT

Eliminado: F

Eliminado: B

Eliminado: E

Eliminado: 9

Eliminado: 0

Eliminado: Average percentage of FeS, FeM, FeD and FeA for the Jökulsá á Fjöllum basin and average amount of each Fe mode of occurrence according to the total content of Fe...

Eliminado: 1

Eliminado: 2

Eliminado: 3

Eliminado: from

Eliminado: from

Eliminado: 4

Eliminado: 5

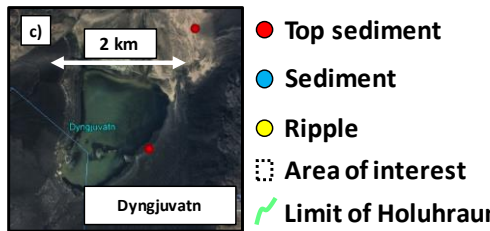
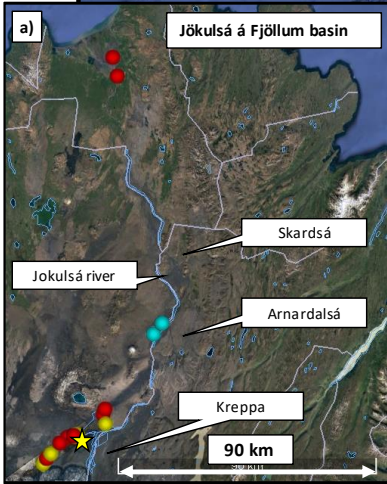
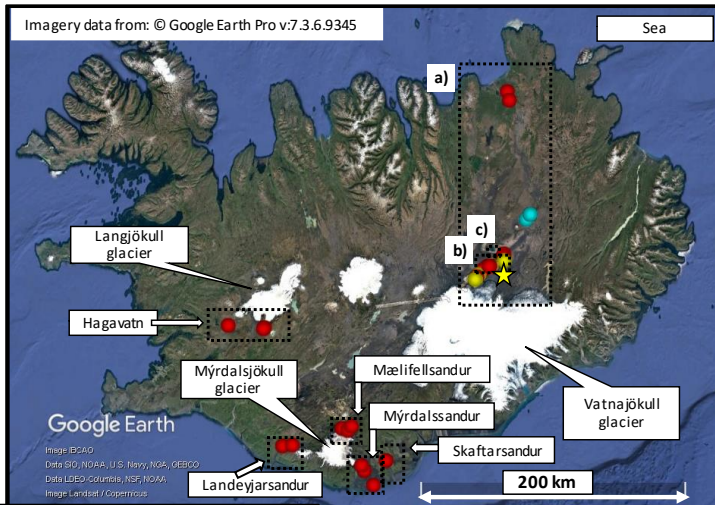
Eliminado: 6

Eliminado: aerodynamic entrainment and saltation bombardment...

1725
1726
1727
1728
1729
1730
1731
1732
1733
1734
1735
1736
1737
1738
1739
1740
1741
1742
1743
1744
1745
1746
1747
1748
1749
1750
1751

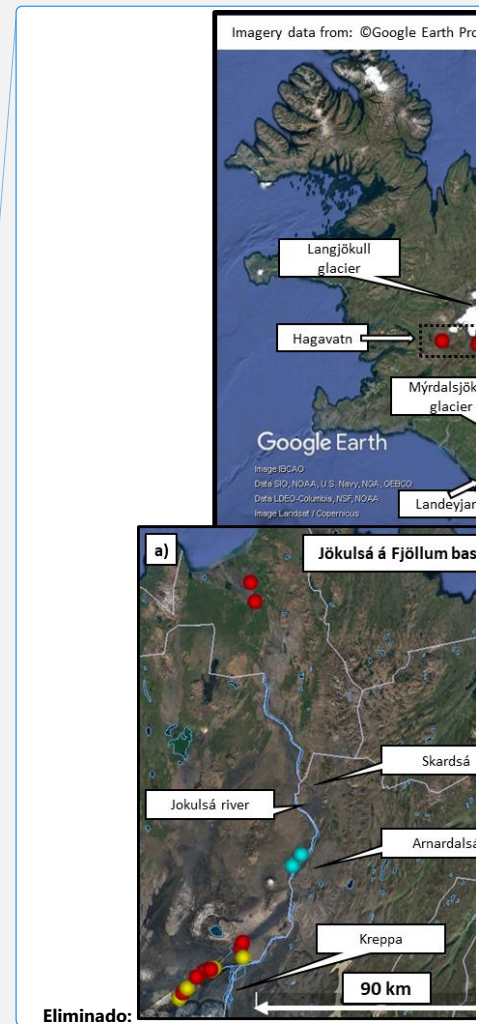
1752
1753
1754
1755
1756
1757
1758
1759

Figure 1.

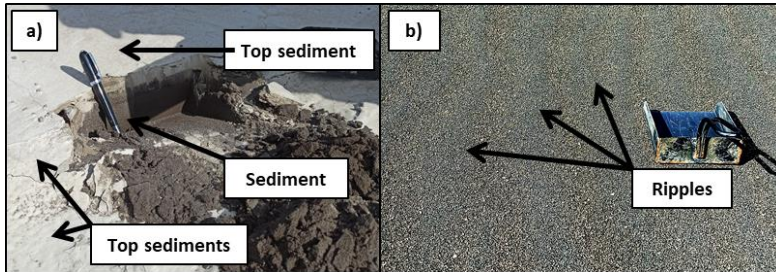


- Top sediment
- Sediment
- Ripple
- ⊞ Area of interest
- Limit of Holuhraun

1760
1761



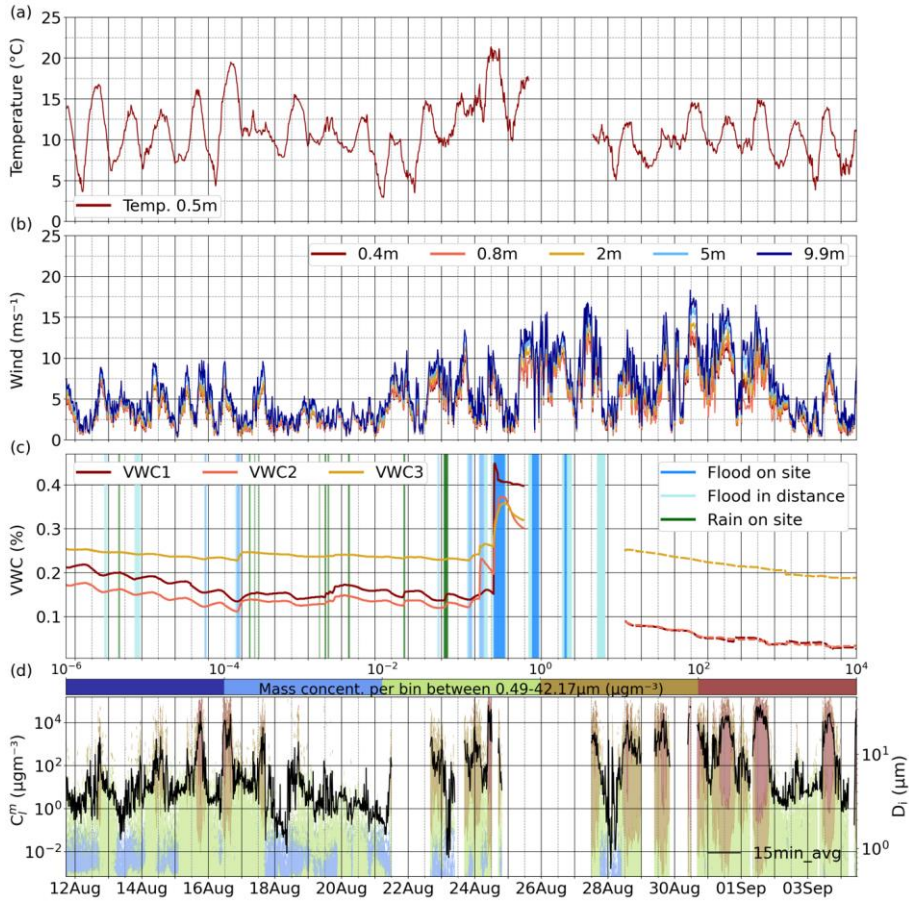
1763 Figure 2.



1764

1765

Figure 3.



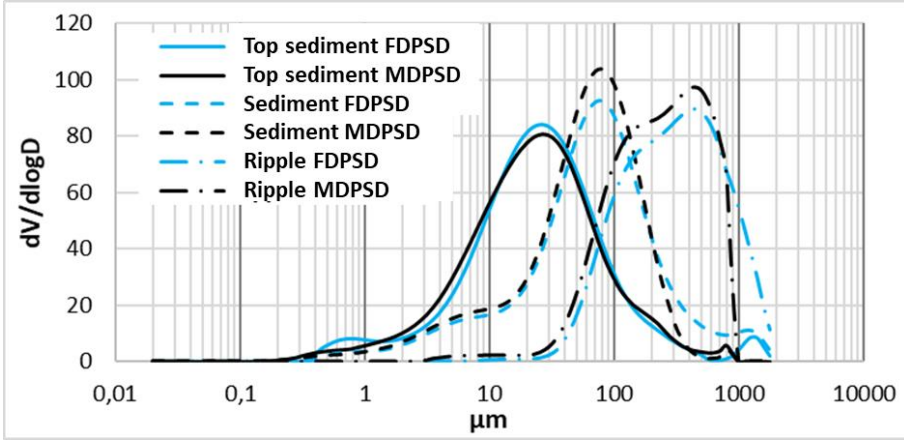
1766

1767

1768

1769

Figure 4.

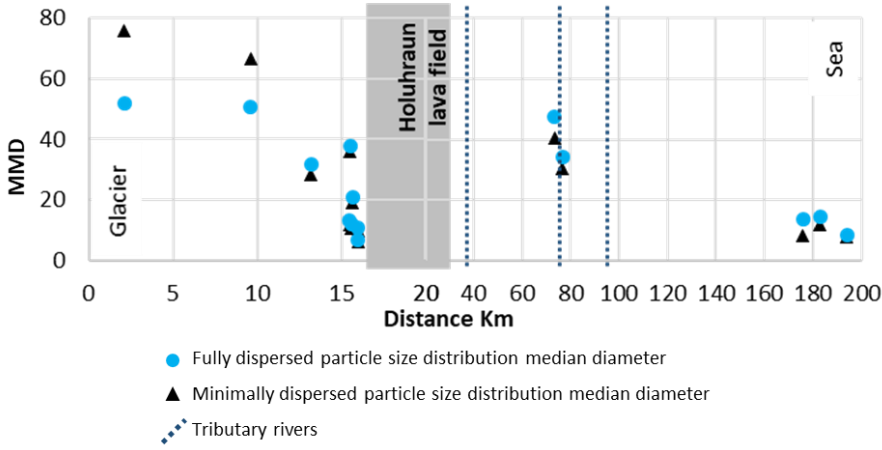


1770

1771

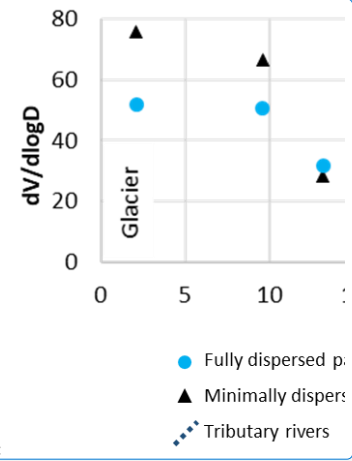
Figure 5

1772



1773

Eliminado: 4

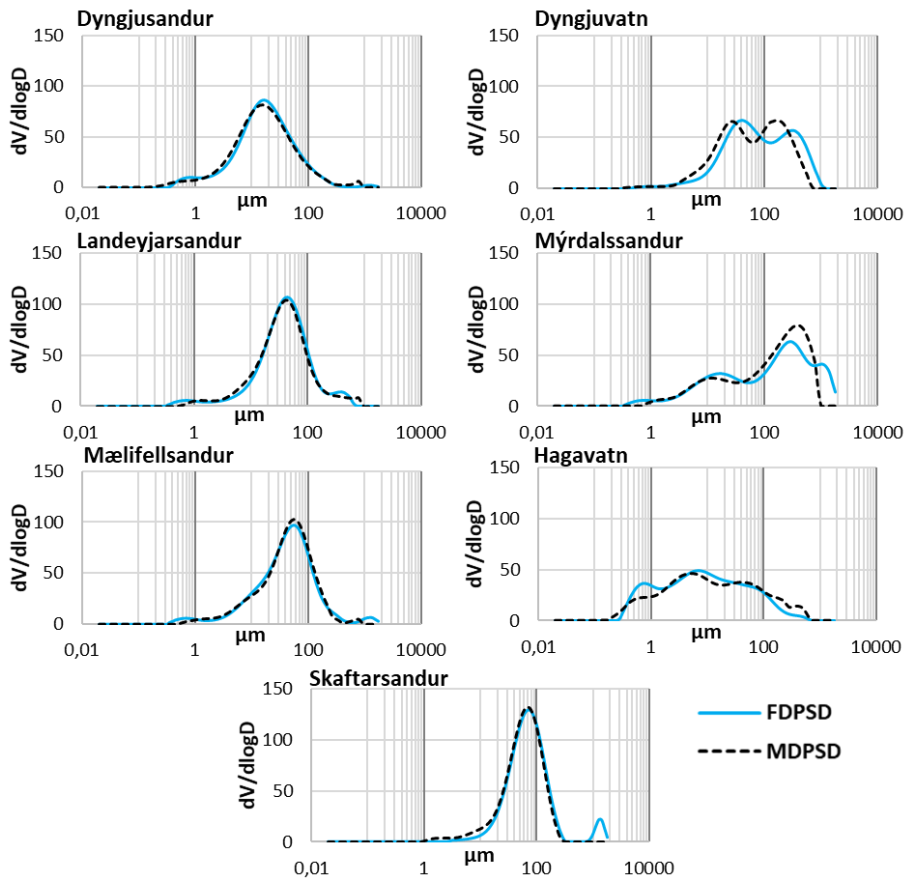


Eliminado:

1776

Figure 5.

Eliminado: 5

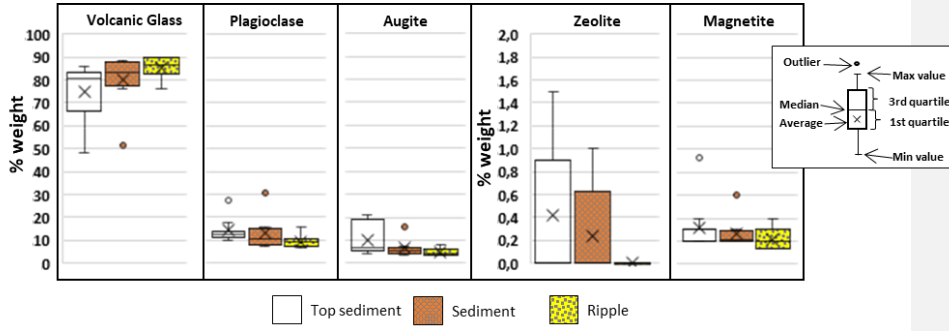


1777

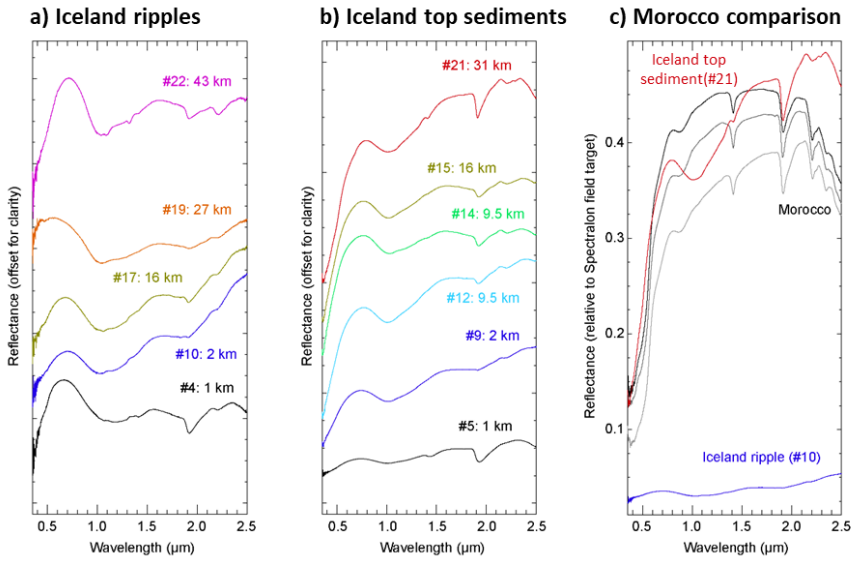
1779

Figure 7.

Eliminado: 6



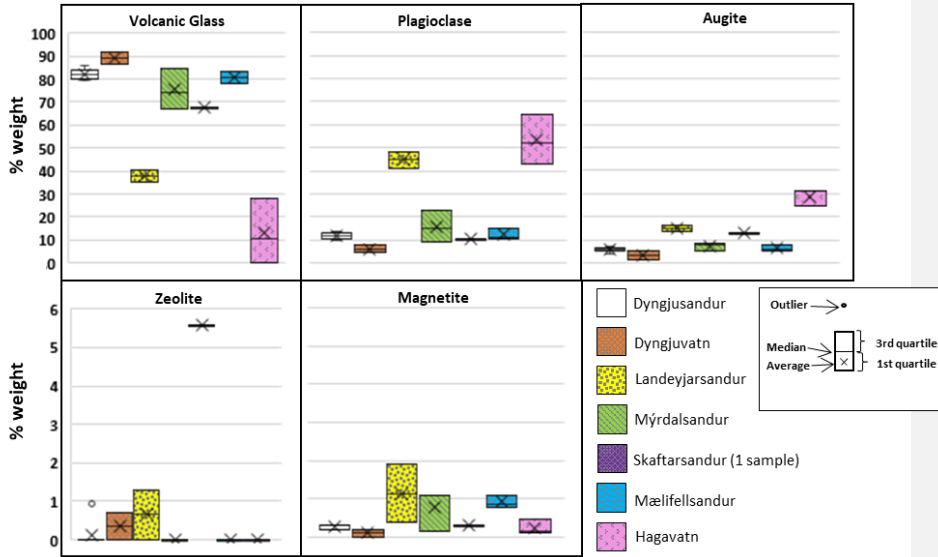
1780



1788

Figure 10.

Eliminado: 9

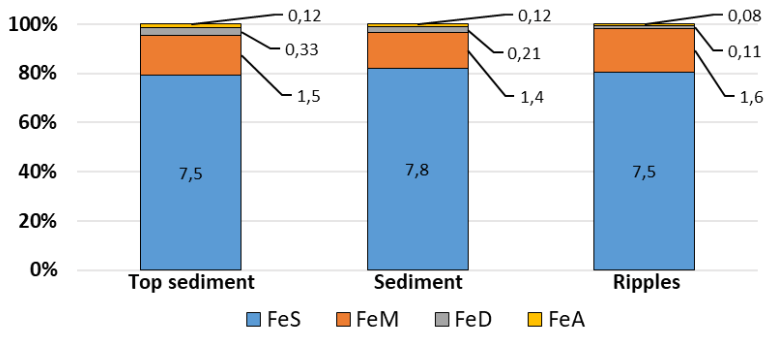


1789

1791

Figure 11.

Eliminado: 10



1792

1794

Figure 12

Eliminado: 1

1795

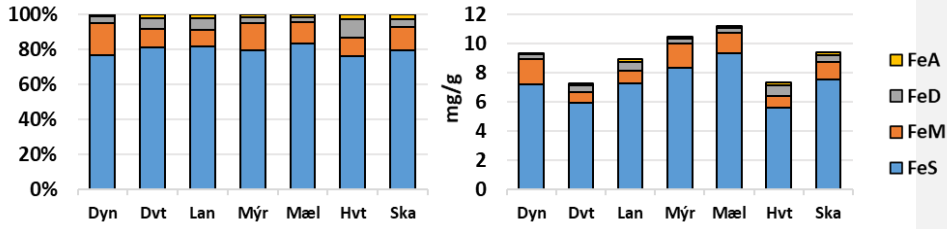
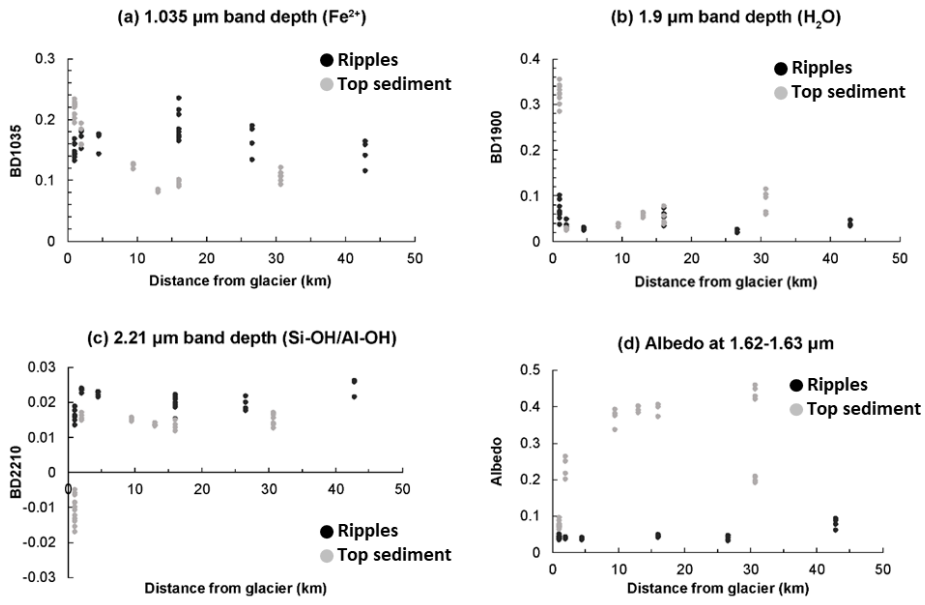


Figure 13.

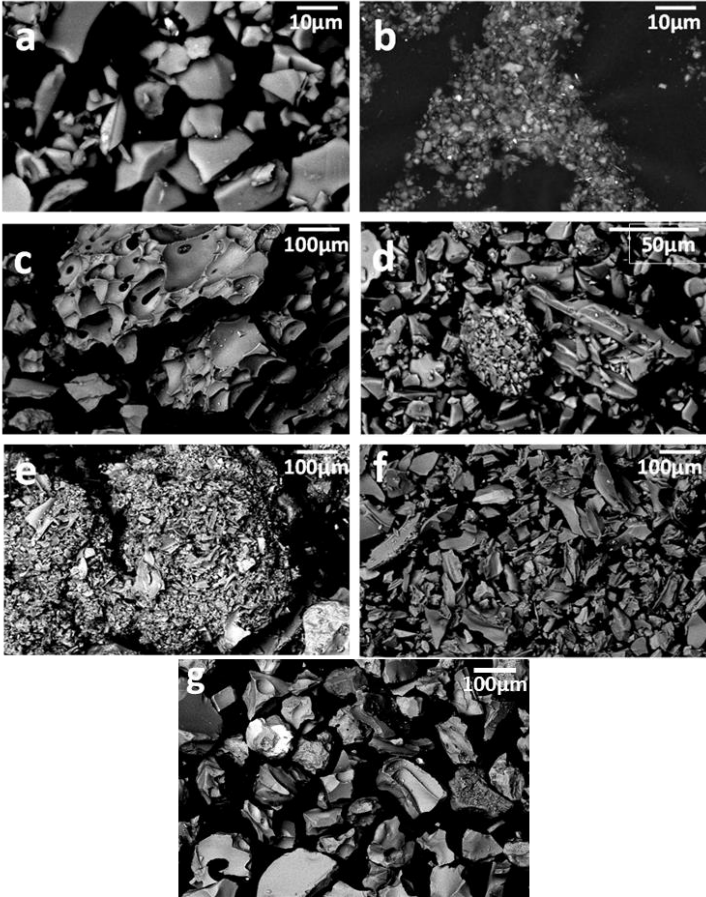
Eliminado: 12



1800

Figure 14.

Eliminado: 13

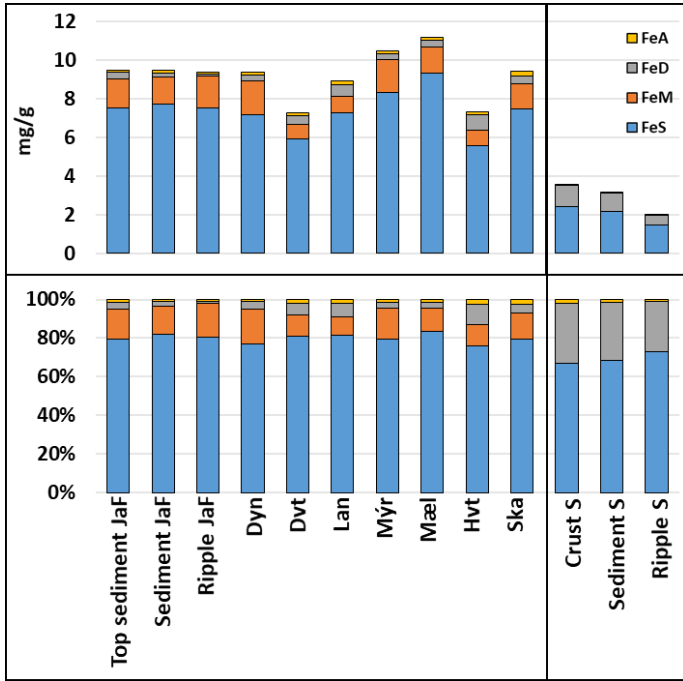


1801

1803

Figure 15.

Eliminado: 14



1804

Figure 16.

Eliminado: 15

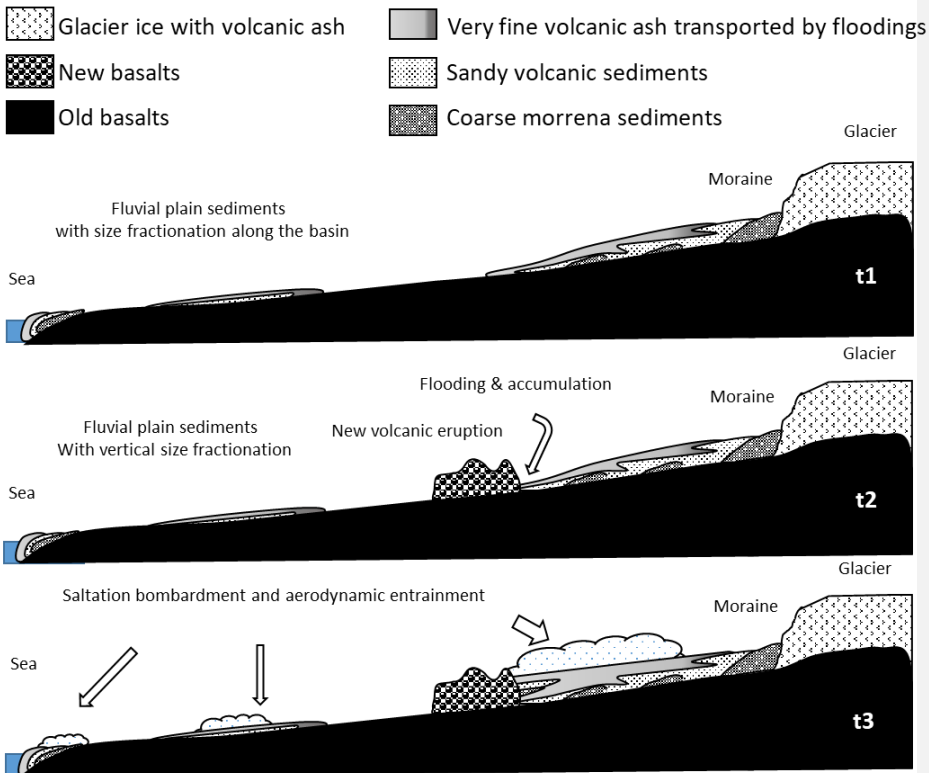



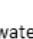


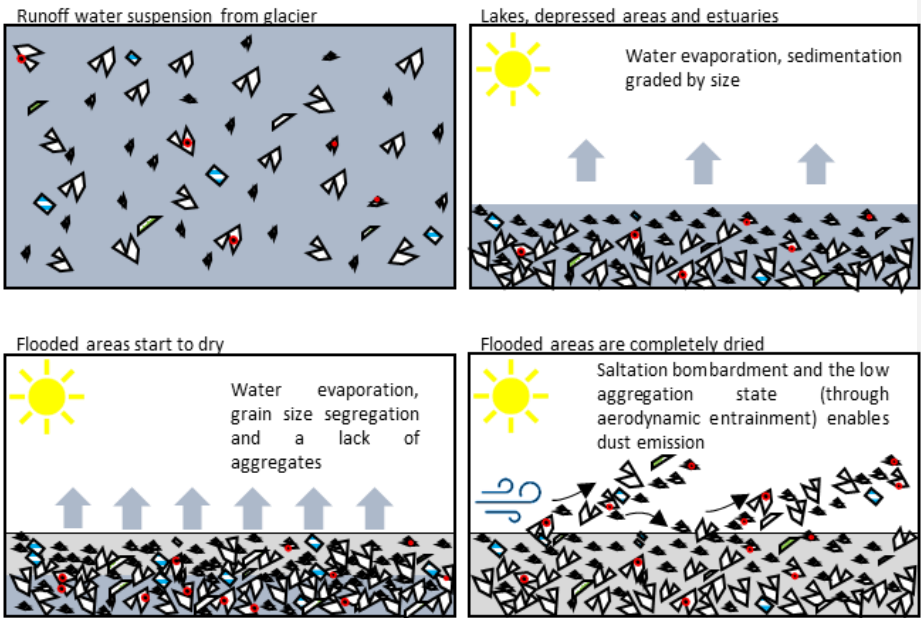


Figure 17.

Eliminado: 16

-  Volcanic glass
 -  Feldspars
 -  Iron oxides (mainly magnetite)
 -  Pyroxenes
-  Water
 -  Dry top sediment



1845

1846
1847
1848
1849

Table 2. Fe mode of occurrence from different locations and types of sample. The content of FeT is in %wt and for every mode of occurrence it is in % of the total Fe content. FeA: content of readily exchangeable Fe, FeD: Fe content from hematite, goethite and pyrite, FeM: Fe content from magnetite, FeS: Fe content from non Fe minerals as Fe-silicates and volcanic glass.

Eliminado: 4

| Location | Type of sample | FeT %wt | FeA % | FeD % | FeM % | FeS % |
|-------------------|----------------|----------|-----------|----------|------------|--------|
| Jökulsá á Fjöllum | Top sediment | 9.5±0.39 | 1.3±0.39 | 3.5±1.5 | 16±5.4 | 79±6.5 |
| Jökulsá á Fjöllum | Sediment | 9.5±0.43 | 1.2±0.44 | 2.2±1.4 | 15±7.8 | 82±8.7 |
| Jökulsá á Fjöllum | Ripples | 9.4±0.41 | 0.85±0.22 | 1.2±0.41 | 18±2.4 | 80±2.4 |
| Dyngjusandur | Top sediment | 9.4±0.21 | 1.2±0.45 | 3.6±1.8 | 18±4.6 | 77±6.7 |
| Dyngjuvatn | Top sediment | 7.3±2.6 | 2.1±0.64 | 7.0±5.1 | 10±3.5 | 81±2.3 |
| Landeyjarsandur | Top sediment | 8.9±0.54 | 1.8±0.67 | 7.2±2.1 | 9.5±3.2 | 81±5.9 |
| Mýrdalssandur | Top sediment | 11±0.41 | 1.4±0.33 | 3.2±1.4 | 16±1.9 | 79±2.3 |
| Skaftarsandur | Top sediment | 9.4±NA | 2.6±NA | 4.4±NA | 13±NA | 80±NA |
| Mælifellsandur | Top sediment | 11±0.48 | 1.3±0.46 | 3.0±0.77 | 12±3.8 | 83±4.8 |
| Hagavatn | Top sediment | 7.4±1.5 | 2.7±1.0 | 10±2.2 | 11±2.4 | 76±4.4 |
| Sahara | Top sediment | 3.6±0.71 | 1.9±0.55 | 31±2.3 | Negligible | 67±2.4 |
| Sahara | Sediment | 3.2±0.47 | 1.4±0.55 | 30±3.0 | Negligible | 68±2.7 |
| Sahara | Ripples | 2.0±0.44 | 1.0±0.54 | 26±5.8 | Negligible | 73±5.9 |

1850